Faculty of Physics and Astronomy
University of Heidelberg

Diploma thesis
in Physics

submitted by
Joachim Welte
born in Karlsruhe

Issued 2007

Single Atom Detection By Fluorescence

This diploma thesis has been carried out by Joachim Welte at the
Kirchhoff Institute for Physics
under the supervision of
Prof. Dr. M. K. Oberthaler

Detektion einzelner Atome mittels Fluoreszenz

In dieser Diplomarbeit wird die Realisierung und Charakterisierung einer magnetooptischen Falle für metastabile ^{40}Ar-Atome beschrieben. Hierzu wird die bereits existierende Vakuumapparatur und das bestehende Lasersystem modifiziert und erweitert.
Die Fluoreszenz von Atomen in der Falle kann mithilfe verschiedener optischer Detektoren (CCD, APD) gemessen werden und dient zur Optimierung der MOT, so dass Einzelatomnachweis über Fluoreszenzdetektion möglich ist.
Die hier dargestellte Messung einzelner Atome wird benötigt, um die Grenzen der Effizienz der bestehenden Apparatur auszuloten. Sie dient somit als Grundstein für den Aufbau eines neuen Experiments und erlaubt eine Abschätzung inwieweit diese Grenzen verschoben werden können und müssen, um den erfolgreichen quantitativen Nachweis des seltenen Isotops ^{39}Ar in natürlichen Wasserproben zu erbringen.

Single Atom Detection By Fluorescence

This thesis describes the realization and characterization of a magneto-optical trap for metastable ^{40}Ar atoms. An existing experimental setup with vacuum apparatus and a laser system is extended and modified to serve this purpose.
Fluorescence of trapped atoms is observed with different optical devices (CCD, APD) and allows optimization of the experimentally accessible parameters to achieve the goal of single atom fluorescence detection.
The recorded single atom signals enable to find the efficiency limits of the present setup and thus have to be seen as the first step of a new experiment. They are used to quantify to which extent these limits may and must be expanded to transfer the newly gained knowledge to the detection of the rare argon isotope ^{39}Ar in natural water samples.

Table 1: Physical constants and properties of argon.

Atomic Mass Unit amu	$1.66053886 \cdot 10^{-27}$ kg	
Planck constant h	$6.626068 \cdot 10^{-34} \frac{\mathrm{m}^2 \cdot \mathrm{kg}}{\mathrm{s}}$	
Boltzmann constant k_B	$1.3806503 \cdot 10^{-23} \frac{\mathrm{m}^2 \cdot \mathrm{kg}}{\mathrm{s}^2 \cdot \mathrm{K}}$	
Bohr magneton μ_B	$9.27400949 \cdot 10^{-24} \frac{\mathrm{J}}{\mathrm{T}}$	
Speed of light c	$2.99792458 \cdot 10^{8} \frac{\mathrm{m}}{\mathrm{s}}$	
Magnetic permeability μ_0	$1.25663706 \cdot 10^{-6} \frac{\mathrm{m} \cdot \mathrm{kg}}{\mathrm{s}^2 \cdot \mathrm{A}^2}$	
Isotope	^{40}Ar	^{39}Ar
Relative abundance	0.996	$8.5 \cdot 10^{-16}$
Mass m	39.96 amu	38.96 amu
Halflife time $\mathrm{T}_{1/2}$	-	269a
Nuclear spin I	0	$+\frac{7}{2}$
Nuclear magnetic moment μ/μ_K	-	-1.3
Relevant transition	$1s_5 - 2p_9$	
Ground state Landé factor g_g	1.506	
Excited state Landé factor g_e	1.338	
Wavelength λ	811.757 nm	
Linewidth γ	$2\pi \cdot 5.85$ MHz	
Lifetime τ	27.09 ns	
Saturation intensity I_0	$1.44 \frac{\mathrm{mW}}{\mathrm{cm}^2}$	
Doppler temperature T_D	141 μK	

Contents

1 Introduction

As climate change has become a major topic in media during the last year the question arises which consequences this change will have for life on earth. In this context one comes to think about the role of water as a limited ressource. The importance of achieving maximum knowledge about the water cycle and the humans' influence on it is thus obvious.
In the past fifteen years huge progress in understanding the importance of ultrasensitive detection of rare isotopes for the analysis of natural samples of different origins has been made, even though the basic knowledge about it exists much longer. The radioactive isotope ^{39}Ar for example allows dating of groundwater and ocean water on timescales of 50-1500 years, in which earth was for sure heavily changed by mankind. It has been proposed for this application several times since the 1970's ([1], [2], [3]).
^{39}Ar is constantly produced in the upper atmosphere by neutron induced spallation of argon, ^{40}Ar(n,2n)^{39}Ar, and hence surface water in contact with the atmosphere has a certain equilibrium concentration. When surface water is sealed from the atmosphere, e.g. is transported in an aquifer, the ^{39}Ar decays and the concentration thus carries information about the age of the water.
One liter of surface water contains only 8500 atoms of ^{39}Ar [4]. The halflife time is 269 years, thus the activity per liter caused by ^{39}Ar is 22 decays/year. This makes simple low level decay counting complicated and longsome [5].
There are several other applicable methods like low level decay counting and different kinds of improved mass spectroscopy, a good overview is given in [6]. The quintessence of that overview is that one method, Atom Trap Trace Analysis (ATTA), is the most favorable, because it can theoretically operate with the smallest sample size, offers the highest selectivity and has a relatively easy and affordable setup.
ATTA is based on magneto-optical trapping of the desired atoms and detecting the fluorescence, which comes from the atom-light interaction. It was first realized in 1999 for Kr isotopes [7] at the Argonne National Laboratory and yielded surprising results like dating sub-saharan groundwater to an age of one million years [8].
This thesis is a first step towards the realization of ATTA for ^{39}Ar: it illustrates the setup of a single atom fluorescence detector that is essential for the long-term objective. The setup of a detection system is chosen since it can be easily tested with the argon beam machine that is normally used for tunneling experiments.

The subsequent chapter gives a brief overview of the theoretical background of magneto-optical traps (MOTs). The parameters and formulas that describe the later presented experiment will be explained and partly derived. The following chapter then explains basic properties of argon and its isotopes. It also describes the experimental setup and the first half of the lab work, namely the design, setup and characterization of a magneto-optical trap for ^{40}Ar. It also features the results from several measurements that clearly motivate how efficiency considerations cause switching between different modes of operation to be necessary.
Chapter 4 presents the main results of the work, which are the successful detection of single atoms in the MOT and the quantitative description of the detection system.
In the conclusion a brief summary of the work done is given and tasks that are subject to further research in order to realize the successful quantitative detection of ^{39}Ar are described.

2 Principles of magneto-optical trapping

This chapter is supposed to sketch how the formulae that are necessary for understanding the principles of the experiment are derived. Due to the limited volume of this thesis, it is not a sufficiently detailed description of the formal approach for readers that are new to the field of atom optics. They are therefore kindly asked to consult reference [9] for a more detailed description of the formal approach and for further insight into the quantum mechanical basis reference [10]. The subsequent derivation of the formulae follows mostly reference [9].

2.1 Quantum mechanical considerations

2.1.1 The Rabi-problem

Since the interaction between atoms and laser light is the heart of this thesis and can be described as the motion of atoms in the light potential, one has to solve the Schrödinger equation (SEQ) for a certain problem, which is in its general time-dependent formulation:

$$H\Psi(\vec{r},t) = i\hbar\frac{\partial\Psi(\vec{r},t)}{\partial t}. \tag{2.1}$$

The Hamiltonian for the field-free and time-independent system is H_0 and the eigenvalues are $E_n = \hbar\omega_n$ with corresponding eigenfunctions $\phi_n(\vec{r})$. Expansion of $\Psi(\vec{r},t)$ in terms of $\phi_n(\vec{r})$ as

$$\Psi(\vec{r},t) = \sum_k c_k(t)\phi_k(\vec{r})e^{-i\omega_k t} \tag{2.2}$$

yields with the Hamiltonian for the interaction $H'(t)$ the equivalent SEQ

$$i\hbar\frac{\mathrm{d}c_j}{\mathrm{d}t} = \sum_k c_k(t)H'_{jk}(t)e^{-i\omega_{jk}t} \tag{2.3}$$

with the integral $H'_{jk}(t) \equiv \langle\phi_j|H'(t)|\phi_k\rangle$ and $\omega_{jk} \equiv (\omega_j - \omega_k)$. This equation is not solvable for the vast majority of physical situation, therefore most closed solutions use approximations.
For the case of laser excited two level atoms one faces the "Rabi Problem". In the

following ground and excited state of the atom are denoted by subscripts g and e, the atomic resonance frequency is defined as $\omega_a \equiv \omega_{eg}$, the laser frequency as ω_l and the detuning δ is $\omega_l - \omega_a$.

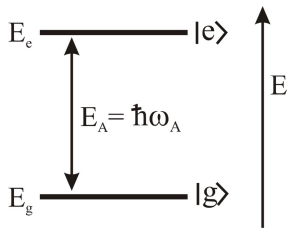

Figure 2.1: The Rabi two level system.

Usually the solution is obtained employing three approximations, where the first one truncates the sum in eq.(2.3) to only two terms representing ground and excited state. $|c_g|^2$ ($|c_e|^2$) then corresponds to the probability to find the atom in the ground (excited) state.
The second one is the rotating wave approximation (RWA): terms in eq.(2.3) that oscillate with ω_l are negligible compared to terms of order δ, because atomic transition frequencies are in the range of 10^{14} Hz whereas typical detunings are in the range of MHz. The rapid oscillations with ω_l average to zero on any relevant timescale.
The third approximation assumes the electrical field of the light to be constant over the region of the integral $H'_{jk}(t)$, that holds because typical wavelengths are 100-1000 nm and the wavefunctions $\phi_n(\vec{r})$ virtually disappear everywhere outside of a sphere with about 1 nm radius (20 times the size of an atom).
Considering the electrical field of the light to be a plane wave in z-direction with amplitude E_0 leads to a coupling strength between the atom and the field $H'_{eg}(t) = \hbar\Omega \cos(kz - \omega_l t)$ with the Rabi frequency defined as

$$\Omega \equiv \frac{-eE_0}{\hbar} \langle e|r|g\rangle \,. \tag{2.4}$$

Further analysis of the equations for c_e and c_g resulting from eq.(2.3) and solving them for the condition that the atom is initially in the ground state, $c_g(0) = 1$ and $c_e(0) = 0$, produces:

$$c_g(t) = \left(\cos\frac{\Omega' t}{2} - i\frac{\delta}{\Omega'}\sin\frac{\Omega' t}{2}\right) e^{+i\delta t/2}, \tag{2.5}$$

$$c_e(t) = -i\frac{\Omega}{\Omega'}\sin\frac{\Omega' t}{2} e^{-i\delta t/2}$$

$$\text{and} \quad \Omega' \equiv \sqrt{\Omega^2 + \delta^2} \tag{2.6}$$

The probabilities for the population of the two states oscillate with the frequency Ω' in time and the amplitude of this oscillation is proportional to Ω^2/δ^2.

$H'(t)$, the part of the Hamiltonian based on the existence of the light field, changes the eigenvalues of the field free system. In the limit $\Omega \ll |\delta|$ the energy shifts are:

$$\Delta E_g = \frac{\hbar\Omega^2}{4\delta} \quad , \quad \Delta E_e = -\frac{\hbar\Omega^2}{4\delta} \tag{2.7}$$

2.1.2 The density matrix

A system with the wavefunction Ψ can alternatively be described by the density operator: $\rho = |\Psi\rangle\langle\Psi|$, expansion of Ψ as in eq.(2.2) yields the elements of the density matrix:

$$\rho_{ij} = \langle\phi_i|\rho|\phi_j\rangle = \langle\phi_i|\Psi\rangle\langle\Psi|\phi_j\rangle = c_i c_j^* \tag{2.8}$$

For the system of interest ρ is a 2x2-matrix and Tr(ρ)=1 because the wavefunctions are normalized. The diagonal elements of ρ are the probabilities $|c_i|^2$ for population and the off-diagonal $c_i c_j^*$'s are so-called "coherences" as they depend on the relative phase between c_i and c_j.
The definition above is valid for a pure state system, i.e. a system where no mixture between the different states occurs. Taking mixtures into account, the density operator looks different:

$$\rho = \sum_i p_i |\Psi_i\rangle\langle\Psi_i|. \tag{2.9}$$

The p_i's are the probabilities to find the system in state i.
When the two-level system is allowed to undergo spontaneous emission from the excited level to the ground state, it changes from being pure state to statistical mixture. This is because spontaneous emission is a random process. The time evolution of a system with the atom being excited and no photon being present at t=0 -denoted as $|e;0\rangle$- is as follows:

$$\Psi(t) = c_{e0} e^{-i\omega_e t}|e;0\rangle + \sum_S c_{g1_S} e^{-i(\omega_g+\omega)t}|g;1_S\rangle. \tag{2.10}$$

Here $|g;1_S\rangle$ corresponds to the atom in ground state while one photon was emitted to the mode S. The formula has to be seen in analogy with eq.(2.2). With the electrical dipole moment $\vec{\mu} = e\langle e|\vec{r}|g\rangle$ and the classical energy density

$$\epsilon_0 \vec{E}_\omega^2 = \frac{E}{V} = \frac{\hbar\omega}{2V} \quad , \text{ zero point energy of field} = \frac{\hbar\omega}{2}, \tag{2.11}$$

equation (2.3) and integrations over time and frequency the subsequent result emerges:

$$\frac{\mathrm{d}c_{e0}(t)}{\mathrm{d}t} = -\frac{\gamma}{2} c_{e0}(t) \quad \text{with } \gamma = \frac{\omega^3\mu^2}{3\pi\epsilon_0\hbar c^3}. \tag{2.12}$$

The probability of the atom to be in the excited state is $|c_{e0}|^2$ and therefore exponentially decays with a lifetime of $\tau = \gamma^{-1}$. In the same manner as the excited state decays the

population of the ground state grows. To obtain the full time evolution of ρ the two terms $(\mathrm{d}\rho_{ij}/\mathrm{d}t)$ from the interaction between light field and atom (eq.(2.5), eq.(2.8)) and from the spontaneous decay are added.
This gives a set of 4 equations, the Optical Bloch Equations (OBE), while using operators and the commutator there is a compact formulation:

$$i\hbar\frac{\mathrm{d}\rho}{\mathrm{d}t} = -[H_0 + H', \rho] + \frac{\mathrm{d}\rho^{sp}}{\mathrm{d}t}. \tag{2.13}$$

Due to the fact that $\mathrm{Tr}(\rho)$=1, the set of equations is over-determined, so there are three equations for independent variables. Solving the OBEs for steady state $(\mathrm{d}\rho/\mathrm{d}t = 0)$ leads to

$$\rho_{ee} = \frac{s_0/2}{1 + s_0 + (2\delta/\gamma)^2} \tag{2.14}$$

with the on-resonance saturation parameter

$$s_0 = 2|\Omega|^2/\gamma^2 = I/I_s \tag{2.15}$$

and the saturation intensity

$$I_s = \pi hc/(3\lambda^3\tau) = \left(1.44\mathrm{mW/cm}^2 \text{ for argon}\right). \tag{2.16}$$

From (2.14) the photon scattering rate is derived:

$$\gamma_p = \gamma\rho_{ee} = \frac{s_0\gamma/2}{1 + s_0 + (2\delta/\gamma)^2} \to \frac{\gamma}{2} \text{ for } s_0 \to \infty,\ s_0/\delta^2 \to \infty \tag{2.17}$$

2.2 Cooling mechanisms

2.2.1 Force on two level atoms

The force on a two level atom resting in a light field can be derived from the Ehrenfest theorem which is in that case

$$F_z = -\left\langle \frac{\partial H}{\partial z} \right\rangle. \tag{2.18}$$

While only the interaction part of the Hamiltonian, $H'(t) = -e\vec{E}(\vec{r}, t)\cdot\vec{r}$, is of interest and the electric dipole approximation is once again applied, the result becomes

$$F_z = e\frac{\partial}{\partial z}\left(\left\langle \vec{E}(\vec{r}, t)\cdot\vec{r}\right\rangle\right). \tag{2.19}$$

Application of the spatial derivative to the term in brackets and eq.(2.4) gives

$$F = \hbar\frac{s_0}{1 + s_0 + (\frac{2\delta}{\gamma})^2}\left(-\delta q_r + \frac{1}{2}\gamma q_i\right) \tag{2.20}$$

where q_r (q_i) is the real (imaginary) part of the logarithmic derivative of the Rabi frequency. For the examined light field q_r corresponds to the gradient of the amplitude and q_i corresponds to the gradient of the phase $(kz - wt)$.
The electrical field of a traveling wave in z-direction with the wave number $k = 2\pi/\lambda$ is $E(z,t) = \frac{E_0}{2}\left(e^{i(kz-\omega t)}\right)$, hence there is no amplitude gradient and with eq.(2.14) and eq.(2.17) one obtains:

$$F_{dis} = \frac{\gamma\hbar k}{2}\frac{s_0}{1 + s_0 + (\frac{2\delta}{\gamma})^2} = \gamma_p \hbar k. \tag{2.21}$$

The second summand in (2.20) can thus be identified with the dissipative light force: it is directly proportional to the photon scattering rate and the transferred momentum per scattered photon. The average of the momenta of the emitted photons is zero, therefore the atom experiences a net force in the direction of the wave propagation.
In the case of a standing wave formed by two counterpropagating waves there is no phase gradient, so q_i is zero and the dissipative force disappears. Closer inspection of the first term in (2.20) then leads to

$$F_{dip} = \frac{2\hbar k\delta s_0 \sin 2kz}{1 + 4s_0\cos^2 kz + (\frac{2\delta}{\gamma})^2}. \tag{2.22}$$

The scenario for atoms in motion is different, a common ansatz uses the OBEs eq.(2.13). For the traveling wave this results in

$$F = F_{dis} - \beta v \quad , \quad \beta = -\hbar k^2 \frac{4s_0(\delta\gamma)}{(1 + s_0 + (\frac{2\delta}{\gamma})^2)^2}, \tag{2.23}$$

with the damping coefficient β. The outcome for the standing wave in the limit $s_0 \ll 1$ is (averaged over an interval of $\frac{\lambda}{2}$)

$$F = -\beta v \quad , \quad \beta = -\hbar k^2 \frac{8s_0(\delta\gamma)}{(1 + (\frac{2\delta}{\gamma})^2)^2}. \tag{2.24}$$

The presence of F_{dis} in eq.(2.23) indicates that the resulting motion is not truly damped towards $v = 0$, because discrete absorption and emission in random directions occur, whereas eq.(2.24) describes a damped motion towards $v = 0$.

2.2.2 1D optical molasses

A system with two counterpropagating beams that are red detuned with respect to the atomic transition frequency, i.e. have a negative detuning δ, causes the atomic velocity along the axis of the beams to be viscously damped and is therefore called “Optical Molasses” (OM).
The velocity dependent force on the atom, which results from the forces of each of the

beams, can be calculated from eq.(2.21) if one takes Doppler-shift due to the detuning into account.

$$F = \frac{\gamma\hbar\vec{k}s_0}{2}\left[\frac{1}{1+s_0+(2(\delta-kv)/\gamma)^2} - \frac{1}{1+s_0+(2(\delta+kv)/\gamma)^2}\right], \vec{k} \uparrow\uparrow \vec{v}$$

Using $r = \delta/\gamma,\ x = vk/\gamma,\ f = F/(\gamma\hbar k)$ for abbreviation gives

$$f(x) = \frac{8s_0 rx}{(1+s_0)^2 + 8(1+s_0)r^2 + 16r^4 + (8(1+s_0) - 32r^2)x^2 + 16x^4}. \tag{2.25}$$

Neglecting any v-dependence in the denominator of eq.(2.25) by setting $x = 0$ and transforming the abbreviations back leads to

$$F = 8\frac{\hbar k^2\delta}{\gamma} \cdot \frac{s_0}{\left(1+s_0+(2\delta/\gamma)^2\right)^2} \cdot \vec{v} \equiv -\beta\vec{v} \tag{2.26}$$

The resulting dependence of the force on the velocity in fig.(2.2), where $r = -1$ and $s_0 = 2$, illustrates that the approximation made in eq.(2.26) holds well for an interval of about $2\gamma/k$ width around $v = 0$, so one defines a capture velocity $v_c = \gamma/k$.
A negative detuning of the light beams results in a cooling force, it is opposed and linearly proportional to the initial velocity and slows down the atom.

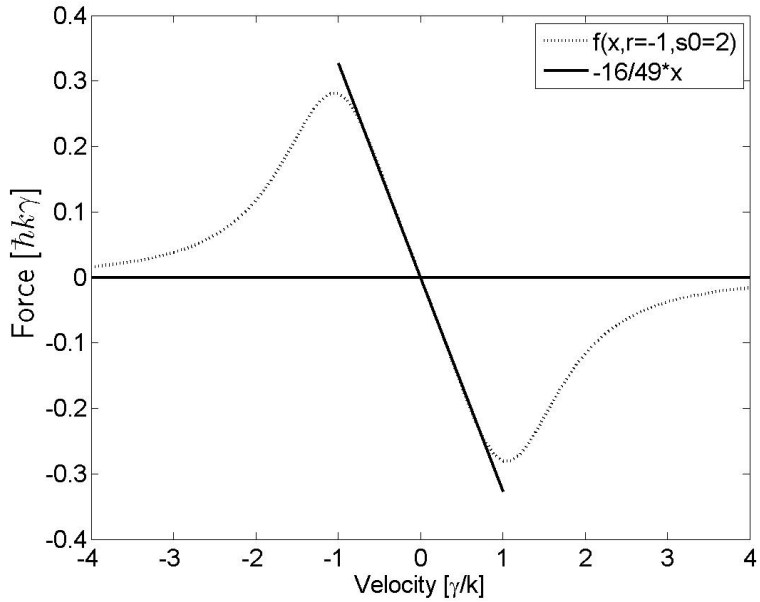

Figure 2.2: The force in an optical molasses as a function of velocity.

It has to be kept in mind that the OM does not describe a trap for atoms: even though their velocity can be damped to a minimum, there is no force that drives them back to a central point.
Due to the absorption of photons, the minimum energy change of the atoms per absorption is $\hbar^2k^2/2M \equiv E_r$, defining the recoil frequency $\omega_r \equiv E_r/\hbar$. The average absorption (emission) frequency is then $\omega_a - \omega_r$ ($\omega_a + \omega_r$). The net energy loss of the light field is therefore $2\hbar\omega_r$, so heating of the atom by $2\hbar\omega_r$ occurs at the rate of $2\gamma_p$ (factor 2 because of the two beams).
The system will reach a steady state, where the cooling at a rate $\vec{F} \cdot \vec{v}$ is just compensate by the heating. This steady state temperature is the minimal temperature

$$T_D = \frac{E_{ss}}{k_B} = \frac{\hbar\gamma}{2k_B}, \tag{2.27}$$

which is also known as the Doppler temperature or the Doppler cooling limit.
Assuming a Brownian motion of the atom in momentum space, the temperature can be related to a diffusion coefficient:

$$T = \frac{D_0}{k_B\beta}. \tag{2.28}$$

The diffusion coefficient arises from a random walk, due to the quantized absorption the stepsize is $\hbar k$ and the step frequency is $2\gamma_p \Rightarrow D_0 = 4\gamma_p(\hbar k)^2$.

$$\Rightarrow T = 4\gamma_p \frac{(\hbar k)^2}{k_B\beta} \rightarrow \frac{\hbar\gamma}{k_B} \quad (s \ll 1, \delta = -\frac{\gamma}{2}). \tag{2.29}$$

2.2.3 Sub-Doppler cooling

From (2.27) the Doppler-limit is estimated for typical linewidths $\gamma \approx 30$ MHz to be $\approx 100\mu K$, but experiments show that significantly lower temperatures are possible. When this was first observed it bred several theoretical concepts two of which are elucidated below [11], [12]. All of these concepts have in commom that they require consideration of the atomic sublevel structure, i.e. here the Zeeman levels.
Both of the examined cooling schemes arise from a configuration of two counterpropagating orthogonally (either linear$\perp$linear or circular/opposite circular) polarized light beams, which form a polarisation gradient field. For linear$\perp$linear beams one finds the polarisation of the field changing from linear to circular to orthogonal to opposite circular to opposite linear on a scale of $\lambda/2$. This represents a strong polarisation gradient. The circular/opposite circular ($\sigma^+\sigma^-$) field has a much smoother transition: here the resulting polarisation is always linear and rotates by 360° over the range of λ.
For a resting atom exposed to a light field the population distribution of the ground state sublevels reacts to the local polarisation and the process of optical pumping ($|g\rangle \rightarrow |e\rangle \rightarrow |g\rangle \rightarrow ...$) lets the excited state distribution follow adiabatically. In contrast

to that, this reaction happens non-adiabatically for moving atoms, because the ground state distribution has to be readjusted continuously to the varying polarisation. This non-adiabaticity is the core of sub-Doppler cooling.
Considering the lin⊥lin-setup and a J_g=1/2 ground state atom in the domain where the polarisation is σ^+, a conveyor-belt-like effect occurs. Absorption of σ^+ photons increases the magnetic quantum number by one ($\Delta M = +1$) while emission allows $\Delta M = -1, 0, +1$. The atom is therefore brought to $M_g = +1/2$. In the σ^- region, the atom is optically pumped to $M_g = -1/2$. While traversing the light field, the atom has to periodically alter between two different ground state distributions. From this periodicity it becomes clear that the associated cooling is the strongest for atoms with a velocity matching the quotient of $\lambda/4$ and the duration of one pumping process.
The light shift is now different from (2.7) but still similar. One finds:

$$\Delta E_g \propto \frac{s_0 \hbar \delta C_{ge}^2}{1 + (2\delta/\gamma)^2} \tag{2.30}$$

where C_{ge} denotes Clebsch-Gordan-coefficients (CGC) [13].
The light shift of $|M_g = +1/2\rangle$ in the σ^+ domain is consequently three times bigger than that of $|M_g = -1/2\rangle$ and vice versa for the σ^- domain. Due to the negative detuning, the shifts are negative. In the σ^+ region, the atom is pumped to $|M_g = +1/2\rangle$ which is the energetically lowest state there. This result can be generalized for all $J_g \rightarrow J_g + 1$ transitions in a way, that the population is always the largest in the state with the largest light shift. Moving to the σ^- region, the atom has to climb a potential hill, because there $|M_g = +1/2\rangle$ lies energetically higher. This transforms kinetic energy to potential energy. In the σ^- region pumping towards $|M_g = -1/2\rangle$ occurs, the atom thus loses the kinetic energy $\frac{2}{3}\frac{s_0\hbar\delta}{1+(2\delta/\gamma)^2}$ and is cooled.
In a $\sigma^+\sigma^-$ setup one does not have a spatially varying type of polarisation, the polarisation is always linear although its direction rotates. Letting the quantization axis of the system rotate in the same manner leads to a system where the light shifts are uniform in space and $\Delta M = 0$ for every transition. To achieve non-adiabaticity, which is necessary for cooling, one needs $J_g \geq 1$. It can be shown that the moving atoms have to undergo optical pumping to countervail the spatial change of the quantization axis, this directly causes non-adiabaticity.
Perturbation theory applied to an atom in motion yields an asymmetric population of the ground state sublevels, traveling towards a σ^+ beam creates higher population of $|M_g = 1\rangle$. The C_{ge}^2 for absorption of σ^+ is six times higher than C_{ge}^2 for the absorption of σ^-, so the atom sees mostly photons opposing its motion and is decelerated.

2.3 The magneto-optical trap (MOT)

2.3.1 Introduction

As shown above, a 1D optical molasses is not yet a trap for atoms, it just slows them down. The reasons are the nonexistence of a central point towards which the atoms are driven and the one-dimensionality. Assuming three pairs of counterpropagating beams, the calculation can be extended to 3D, but solving the problem becomes more complicated. The central point can be created by applying a magnetic gradient field.
Two coils with opposite current circulation realize a quadrupole field. The following comments hold for the z-axis, which is perpendicular to the coils. In the center of this configuration the zeroth and the second derivative of the resulting magnetic field are zero due to the symmetry. If one chooses the distance of the coils to be $\sqrt{3}$ times the radius of each of the coils, the third derivative is likewise zero: in the vicinity of the center the magnetic field is linearly dependent on the distance from the center, $B(x) = A \cdot x$.
From atom physics [14] one knows that this leads to Zeeman-shifts of the magnetic sublevels. On account of the magnetic field gradient, these shifts depend on the position in the field as indicated in fig.(2.3) for an atom with $J_g = 0$ and $J_e = 1$.

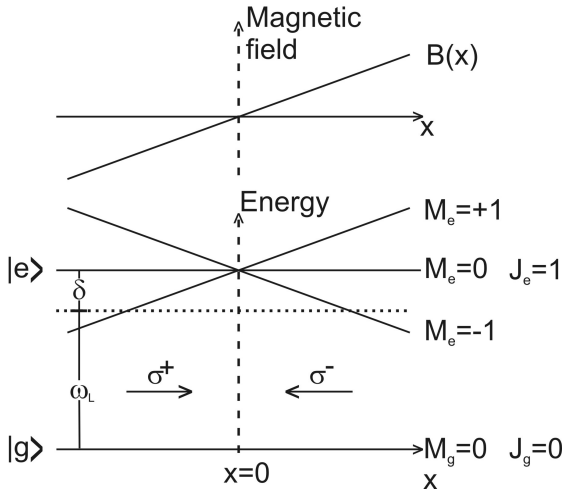

Figure 2.3: Beam setup in a one dimensional MOT.

For the $\sigma^+\sigma^-$ design the resulting detuning makes an atom interact only with one beam at a time, if the polarisations are in the right way, this yields a dissipative force directed towards the center. Interaction with σ^+ maximizes the population of the sublevel with the highest M, whereas interaction with σ^- redistributes the atoms mainly to the lowest M, thus forming a closed transition in each case. The atoms are then cooled in momentum space and trapped in real space, which defines a trap. As above, this can be expanded to any $J_g \to J_g + 1$ transition.

2.3.2 Temperature and size

Analog to the derivation of (2.26), (2.21) is modified with respect to the different detuning: $\delta' = \delta \mp kv \pm \mu' B/\hbar$ where $\mu' = (g_e M_e - g_g M_g)\mu_B$ is the effective magnetic moment and the g_i are the Landé-factors. Approximating the resulting expression in the low intensity limit for small Doppler- and Zeeman-shifts gives

$$\vec{F} = -\beta\vec{v} - \kappa\vec{r} \quad , \quad \beta : \text{damping coefficient as defined in (2.26)} \tag{2.31}$$

$$\kappa = \frac{\mu' A}{\hbar k}\beta \quad , \quad A : \text{magnetic field gradient.} \tag{2.32}$$

κ represents the proportionality factor of a force dependent on the distance from the center and is therefore identified as a spring constant. Rewriting the equation in a different way for the one dimensional case clarifies this immediately:

$$\ddot{x} + \frac{\beta}{M}\dot{x} + \frac{\kappa}{M}x = 0 \tag{2.33}$$

The differential equation describes a damped harmonic oscillation with damping rate $\Gamma = \beta/M$ and oscillation frequency $\omega_r = \sqrt{\kappa/M}$. Typical values (e.g. $1s_5 - 2p_9$ transition of Ar) lead to $\Gamma \approx$100kHz and $\omega_r \approx$kHz. This allows the conclusion that an atom follows an overdamped oscillation around the center of the trap.
Thermodynamical equipartition of the energy of the atom produces a relation between temperature, average velocity and average deviation from the center position:

$$k_B T = m v_{rms}^2 = \kappa z_{rms}^2. \tag{2.34}$$

Evaluated for typical values, this gives a MOT size of a few hundred μm. The combination of (2.28), (2.26) and (2.34) yields:

$$z_{rms}^2 = \frac{\hbar\gamma^3}{32k\mu' A} \cdot \frac{(1 + s_0 + (2\delta/\gamma)^2)^3}{s_0\delta^2}. \tag{2.35}$$

From partial derivation of this expression the MOT size is found to be minimal for $s_0 = 1$ and $|\delta/\gamma| = 1/2$.

3 Experimental realization for ^{40}Ar

3.1 Basic properties of ^{40}Ar

Argon is a noble gas and therefore chemically inert. Its atomic number is 18 and it has several isotopes with masses ranging from 35 amu to 44 amu. The isotopic composition is mainly monoisotopic: 99.6% Ar-40, 0.33% Ar-36, 0.06% Ar-38. There are several very rare radioisotopes. Ar-39 for instance has a relative abundance (upon total Ar) of $8.5 \cdot 10^{-16}$ [4]. The three mentioned natural isotopes have vanishing nuclear magnetic momenta, because they have even-even cores, whereas Ar-39 does have $I = +\frac{7}{2}$. Due to $\mu = I = 0$ there is no hyperfine structure in Ar-40: hyperfine structure is based on the coupling of the total angular momentum of the electrons to the nuclear magnetic moment.

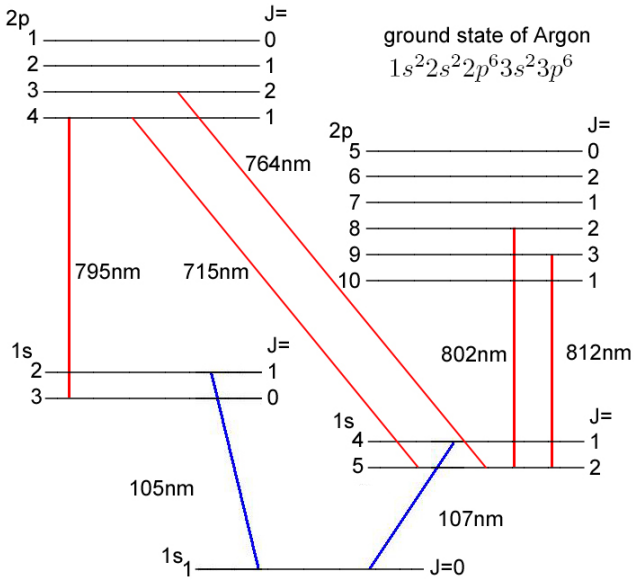

Figure 3.1: Simplified Ar-40 level scheme in Paschen notation.

The ground state of Ar-40 is $1s^2 2s^2 2p^6 3s^2 3p^6$ with completely filled outer shells that are characteristic for noble gases. Ar-40 has two metastable levels which are of particular interest, they are reached by exciting one of the $3p^6$ electrons to $4s$. In Paschen-notation they are denoted as $1s_3$ and $1s_5$ with lifetimes of 45 seconds and 38 seconds, respectively. Paschen notation numbers the energy levels consecutively starting from the energetically highest. There are several transitions in the infrared from those levels to higher ones, e.g. the $4s$ electron can be transfered to $4p$ by 811.757 nm [15]. This is the transition that is always referred to below. It is -beside other transitions- indicated in fig.(3.1).
$1s_5 - 2p_9$ is a closed transition, the probability to decay from the upper level $2p_9$ to the lower $1s_5$ level is unity for all practical purposes. The linewidth is $\gamma = 2\pi \cdot 5.87\text{MHz}$ [9]. The importance of such a closed transition for capturing atoms becomes clear if one thinks of an open one where atoms will decay to states different from the initial "ground"-state, if no additional laser is used the atom can no longer be manipulated, because it does not see the light anymore.

3.2 Generation of the atom beam

3.2.1 Vacuum system

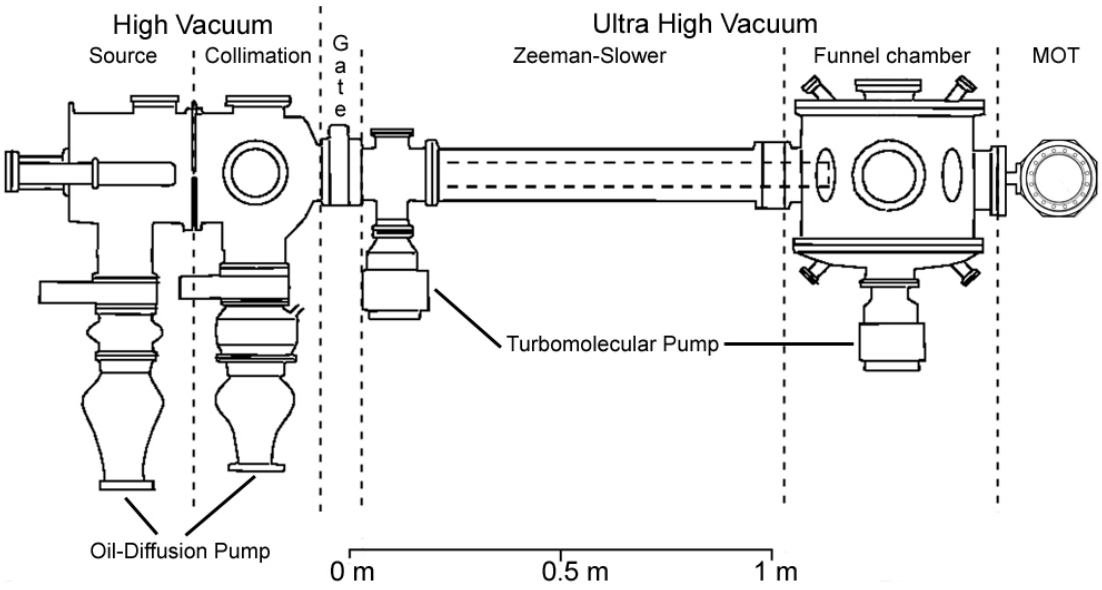

Figure 3.2: Scheme of the vacuum system.

The vacuum part of the experimental setup can be divided in different ways as it can be seen in fig.(3.2). First of all, one distinguishes the high vacuum part (HV) from the ultra high vacuum part (UHV). The HV part again consists of two different components: the

atom source and the collimation chamber. Attached to each of the chambers is an oil diffusion pump, the pumping speed of the first pump is 2350 l/s, the second one pumps 700 l/s.
The pressure in the atom source chamber is the highest in the system when the argon intake is open, ranging from about 10^{-3}mbar in the source to $2 \cdot 10^{-5}$mbar in the rest of the chamber. From the pumping speed and the pressure maintained during operation one estimates the argon flux to

$$\dot{N} = \frac{2350\frac{l}{s} \cdot 2 \cdot 10^{-5}\text{mbar}}{1.38 \cdot 10^{-23} J/K \cdot 300K} \approx 10^{18} s^{-1}. \tag{3.1}$$

A second approximation for the argon consumption can be obtained from the lifetime of a 50l/200bar Ar gas bottle, which is about 1.5 years:

$$\dot{N} = \frac{50l \cdot 200\text{bar}}{4.7 \cdot 10^{7} s \cdot 1.38 \cdot 10^{-23} J/K \cdot 300K} \approx 5 \cdot 10^{18} s^{-1} \tag{3.2}$$

If one bears in mind that the argon is continuously -even if the experiment is not running- pumped away in order to keep the spectroscopy cells at a sufficiently low pressure (explained later), one finds that only one fifth of the total argon consumption is due to the generation of the atom beam.
With no argon input, the pressure in the first chamber is as low as 10^{-7}mbar. The collimation chamber and the source chamber are separated by an aperture of about 3mm diameter. This works as a differential pumping stage and leads to pressures in the collimation chamber of $\approx 10^{-6}$mbar.
The HV region of the apparatus is separable from the rest by a gate valve, this allows frequent maintenance of the source without venting the UHV part of the machine. Pumping down the HV takes -heating up included- only one hour thanks to the high pumping rates of the oil diffusion pumps. The gate valve can also be used to decrease the flux of atoms which proves useful for single particle detection.
In the UHV zone two turbo-molecular pumps (300l/s) constantly evacuate to $10^{-8} - 10^{-7}$mbar depending on the argon input. In the discussion of the vacuum setup, the Zeeman-slower can be treated as a simple tube, its function is illustrated below in the section dealing with the optical system. The funnel chamber is not important in the present experiment, its existence in the setup is based upon a second experiment which is also performed on the apparatus by L. Kierig, A. Schietinger and J. Tomkovic.
The investigated experiment takes place in the last chamber, which is hence referred to as the "MOT-chamber". This part was newly installed during this diploma work. It is CNC-machined from unitary stainless steel 304 by Kimball Physics Inc. and was chosen because of its very compact design: the diameter of the octogonal base area is 178mm, compared to the diameter of the mounted CF100 windows (152mm), this comes close to the smallest possible. The superficies surface is even closer: the height of the component is 71mm, the eight mounted CF40 windows have each a outer diameter of 70mm.

The chamber is vertically oriented and connected to the funnel chamber via a CF100-CF40 reducer with 70mm length. This configuration grants the maximum number of accessible ports and is ideal for the application as MOT chamber, because in that way three pairs of both rigidly mounted and well adjustable counterpropagating laser beams can easily be generated.

3.2.2 Atom source

As explained above, the experiment uses the metastable $1s_5$-state as "ground" state for laser transitions. This results in the necessity of an efficient excitation of ground state atoms to that state. Electron impact excitation fulfills that condition and is achieved by a DC gas discharge of argon which produces a sufficient amount of free electrons. These electrons are accelerated in a second stage and excite ground state argon atoms to all kinds of upper levels while passing the acceleration stage. As $1s_5$ is populated directly by some of the atoms and some others decay from upper levels to it, one gets an adequate fraction ($\sim 10^{-4}$) of metastable atoms.
The efficiency of this process can be estimated with the help of [16]. Integration of eq.(4.3) from [16],

$$I(\theta)\mathrm{d}\Omega = \frac{\mathrm{d}}{\mathrm{d}t}N(\theta) = \frac{1}{4\pi}n\overline{v}\sigma\cos(\theta)\mathrm{d}\Omega, \tag{3.3}$$

(n: density, σ: exit aperture, $\overline{v}$: peak velocity) in the interval $\theta = [0, \pi/2]$ and $\phi = [0, 2\pi]$ yields a total flux of metastable atoms

$$\dot{N} = \pi\eta_e I(0) \quad , \quad I(0)\text{: intensity in forward direction, } \eta_e\text{: excitation efficiency.} \tag{3.4}$$

In that thesis $I^{theo}(0) = 6 \cdot 10^{13}(\mathrm{sr}\cdot\mathrm{s})^{-1}$ and $\eta_e \approx 0.03$ were determined, this gives $\dot{N} = 10^{13}$. Comparing this to (3.1) one finds the total efficiency of the source to be $\eta \approx 10^{-5}$. The aperture between collimation chamber and Zeeman slower limits the flux of atoms. Its area is roughly $1\mathrm{cm}^2$ while the distance from the source is about 30cm. The solid angle is thus 10^{-3}sr, that leads to 10^9 atoms/s. The collimation (see below) increases the flux in forward direction by a factor of 100, hence 10^{11} atoms enter the Zeeman slower per second. Compared to the previous calculation the overall efficiency between source and Zeeman slower is 10^{-7}. The velocity of the atoms emitted by the source follows a Maxwell distribution with its peak at 310m/s.
The aim of this thesis is the detection of single atoms making it indispensable to reduce the efficiency of the apparatus. In this context the source was tilted, because (3.3) clearly shows an angular dependency of the flux.

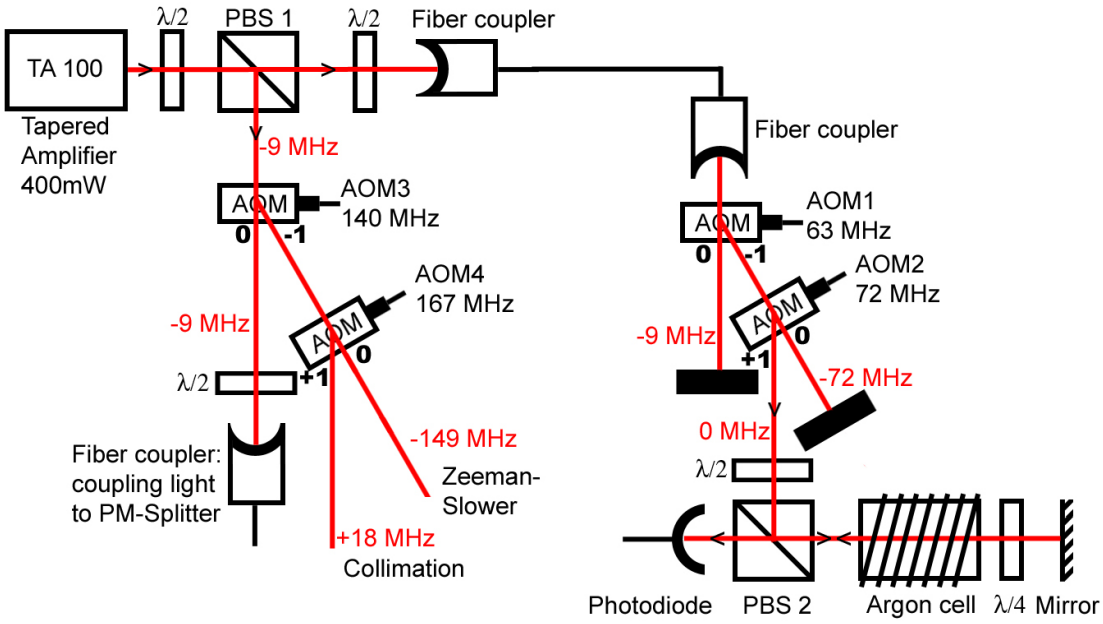

Figure 3.3: Scheme of the laser setup. Numbers in red indicate the detuning of the beams relative to the atomic transition, bold numbers indicate the diffraction order.

3.3 Optical components

3.3.1 Laser system

The most important component of the laser system sketched in fig.(3.3) is the 400mW tapered amplifier laser (TA100 @ 811.757nm) located on a breadboard that is attached to the frame of the vacuum machine. The shape of the beam emitted by the present laser is not gaussian, but could probably reshaped with an appropriate optical setup.
Directly behind the exit of the laser, the beam is split via a polarising beam splitter (PBS1) in two beams: one for the spectroscopy and the other one for the experiment. The $\lambda/2$-waveplate preceding PBS1 allows power adjustment. The spectroscopy beam is then coupled to a polarization maintaining singlemode fiber and transferred to an optical table, where it is uncoupled from the fiber. Passing an acousto-optical modulator (AOM) with a driving frequency of 63 MHz the beam ideally experiences Bragg diffraction. An AOM is a crystal in which a travelling sound wave is excited by a piezo attached to one side of the crystal. To the opposite side an absorber is connected, it ensures that no standing wave can occur. The wave transfers $\pm n\hbar k_{AOM}$ to the photons, this detunes the -1st diffraction order by -63MHz relative to the light emitted by the TA100. This beam is sent through a second AOM ($\nu = 72$MHz), here the +1st order is of interest, which is $(72 - 63)$MHz $= +9$MHz detuned.

Doppler-free saturation spectroscopy [17] is used to lock the +1st diffraction order of AOM2 on the $1s_5 - 2p_9$ transition of argon, thus locking the TA100 to $\nu_{1s_5-2p_9} - 9$MHz. The spectroscopy cell is filled with argon at a pressure of ≈0.1mbar, where a RF-discharge is maintained by a tuned circuit and the $1s_5$ level is populated. The beam coming from AOM2 works as pump beam, the probe beam is the same but reflected by a mirror and with orthogonal polarisation. The rotated polarisation is achieved by traversing a $\lambda/4$-waveplate with axes oriented 45° to the incident polarisation twice. It is necessary for separating the probe from the pump beam: due to the orthogonal polarisation, PBS2 reflects the pump beam but it transmits the probe beam.
When the laser frequency is scanned over the resonance, the monitor signal shows a Doppler absorption profile. Due to the random motion of atoms in the gas cell, which leads to random Doppler-shifts, there are always atoms that are resonant with the current frequency. Located in the minimum of the observed transmission there is a peak: the Lamb dip (dip refers to absorption). It appears when the laser is resonant with atoms of velocity $v = 0$, because in that case the pump beam, which is at saturation intensity, brings 50% of the atoms with $v = 0$ to the excited state and the probe beam can no longer be absorbed by those atoms.
To stabilise the laser on the Lamb dip, deviations in frequency have to be corrected, that can be done by usage of the lock-in-technique: The current of the laser is modulated with a high frequency (≈30kHz), therefore the monitor signal has the same modulation. The monitor signal is electronically multiplied with the modulation frequency, the product is integrated and the integral yields -if the right integration time is chosen- the derivative of the signal. This derivative is fed into a PI-loop as an error signal and is used to lock the laser to resonance.
In the second optical path starting from PBS1 the setup of the AOMs is identical to that in the first path, except for the fact that all diffracted beams are used and the driving frequencies of the AOMs are roughly twice as high. The undiffracted beam of AOM3 is coupled to a "Polarisation Maintaining Fiber Splitter 1x4" (PMS), which distributes the input laser power among four output channels under conservation of the linear polarisation. Three of these are used for the MOT while one is used for monitor purposes. The coupler has a focal length $f = 15.3$mm and the Nufern PM-780-HP fibers of which the PMS is built have a numerical aperture $NA = 0.128$@812 nm. The core diameter of the fiber can be identified with mode field diameter (MFD). It is related to the radius of the beam at the fiber end (waist w_0) by $w_0 = 0.82\text{MFD}/2$. The MFD is 5μm, so w_0= 2μm. There is also a simple relation between beam radius (13.5% waist = e^{-2}-value) R, focal length f and numerical aperture (5% value=e^{-3}-value) NA:

$$R = \sqrt{\frac{2}{3}} NA \cdot f. \tag{3.5}$$

Thus the entrance diameter of the beam is determined to 3.2mm.
The polarisation maintenance can be tested by applying either mechanical (bending) or thermal (heat) stress to the fibers and monitoring the variation of the output power

with a polarisation sensitive device (e.g. a PBS). It was found to be within acceptable tolerances: $\sigma \leq 2\%$. The monitor channel also allows to check the total laser power variation during operation of the MOT, which was found to be $\sigma \leq 3\%$.
The output fibers are numbered for convenience, when the device was first tested using a TiSa-laser with a clean beam profile, the following output powers were measured as in tab.(3.1)

Table 3.1: Measured performance of the PM-Splitter.

Output	1	2	3	4	$\sum$
Power[%]	11	9.5	11	12	43

As the power should be approximately the same in each of the MOT beams, output channel #2 is chosen as monitor. As mentioned above, the TA100 does not produce a perfect gaussian mode, but a combination of several modes. This decreases the efficiency of fiber coupling by a factor of 5 (measured) compared to coupling TiSa-light.
Light passing AOM4 is partly diffracted to the -1st order, which then has +18MHz detuning. This beam can be used for collimation of the atom beam and is discussed below. The non-diffracted part of the light is -149MHz detuned from the atomic resonance and is utilised in the Zeeman-slower. This is also explained in the following section.

3.3.2 Deceleration and collimation of the atoms

The setup of the apparatus offers the possibility to manipulate the atom beam with light in two ways: it can be collimated, meaning reduction of the transversal atomic velocity, and it can be longitudinally slowed.
Collimation takes place in the second vacuum chamber, where a laser beam is continuously reflected between two tilted mirrors. In this thesis, the collimation was always blocked. It causes a much higher flux in forward direction of the beam, which increases the number of atoms in the MOT. Dealing with the task of detecting single atoms of a very frequent argon isotope too high fluxes have to be avoided.
Longitudinal slowing shifts the peak of the Maxwell velocity distribution to lower velocities. The technique is similar to that of the MOT: a spatially dependent magnetic field results in a spatially varying effective detuning due to the changing Zeeman shift. Combined with a laser beam counterpropagating the atoms this can be used to decelerate the atoms in longitudinal direction. When the Zeeman slower is optimally adjusted, it decelerates the atoms from $\overline{v} = 310$m/s to about 40 m/s. As already mentioned, a high flux of atoms that can be captured is not favorable, so the Zeeman-Slower is not really needed for single atom Ar-40 measurements: even if it is switched off, there are still sufficiently many slow atoms in the tail of the Maxwell-Boltzmann distribution.

3.3.3 MOT beams

Each of the three chosen outputs of the PMS is plugged on a homemade fiber collimator: an adjustable plate with a thread on which the FC-APC fiber connectors are screwed, then a rotatable $\lambda/4$-plate to change from linear polarisation to circular, then in a distance from the fiber end slightly more than its focal length a lens with f=50mm. With eq.(3.5) the beam diameter is computed as 10.5mm. The beams are not perfectly collimated, which proves useful because the later discussed second $\lambda/4$-plate per beam has the same diameter as the lens: a perfectly collimated beam would inevitably lead to disturbing scattering of photons, this has to be avoided for single atom fluorescence detection.

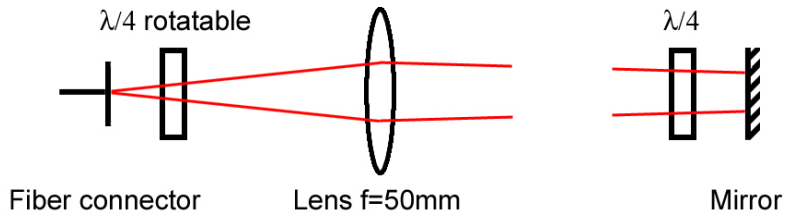

Figure 3.4: Selfmade outcoupler for MOT beam collimation.

The MOT is a so-called "retroreflected beam MOT": there are not six independently adjustable paired beams, but only three beams which cross the MOT and are retroreflected on the opposite side with an adjustable mirror (high reflection coating for 700-1200nm). Directly in front of each mirror there is a $\lambda/4$-plate as indicated in fig.(3.4). Those are necessary for the desired $\sigma^+\sigma^-$ setup, which consists of two counterpropagating beams with the same rotational direction of the -ideally circular- polarisation. The mirror induces a 180° phase shift of each component of the polarisation vector, so it transforms lefthand polarisation to righthand polarisation and vice-versa. With the waveplates the phase shift can be compensated and incident lefthand polarisation is reflected as lefthand polarisation.
In that case the original beam and its reflected counterpart have the same polarisation but opposite sense of propagation, this is summarized in the σ^+/σ^- notation.

3.4 Magnetic field

3.4.1 Design of the coils

As mentioned above a magnetic quadrupole field produced by a pair of identical -besides the direction of winding and respectively direction of current - coils is used. Due to the geometry of the field the circular polarisation on the axis perpendicular to the coils has to be orthogonal to that on the axes parallel to the coils in order to achieve a compressing

force. The axial field of two coils can easily be calculated with the Biot-Savart law:

$$B(x) = \frac{\mu_0}{2} InR^2 \left[\frac{1}{(R^2 + (d/2 + x)^2)^{3/2}} - \frac{1}{(R^2 + (d/2 - x)^2)^{3/2}} \right], \tag{3.6}$$

n: windings, R: radii, I: current and $d/2$: distance from origin. In a Taylor expansion for $x = 0$ the field is dominated by the first spatial derivative

$$B'(0) = \frac{-3\mu_0}{2} InR^2 \frac{d}{(R^2 + (d/2)^2)^{5/2}}. \tag{3.7}$$

The second derivative is zero at $x = 0$, linearity of the field requires that the third spatial derivative at positon $x = 0$ disappears, this yields a simple relation between coil radius and distance of the coils: $d = \sqrt{3}R$.
Experimental constraints do not allow free choice of all parameters: the MOT size is proportional to $A^{-1/2} \equiv B'(0)^{-1/2}$ as in (2.35) and d cannot be less than 130mm because of the geometry of the MOT chamber (height(Kimball) + 2 · height(CF100-window)).
The power consumption of the coil pair can be calculated by rewriting eq.(3.7)

$$nI = \frac{-2}{3\mu_0} \frac{(R^2 + (d/2)^2)^{5/2}}{dR^2} A. \tag{3.8}$$

Eq.(3.6) is an approximation of the field for coils being flat and thin compared to their radius and distance. The area covered by the coil windings is thus set to $p^2 \cdot d \cdot R$, in the following p=0.12. Because the windings are made of round wire this area cannot be completely filled, the area filling factor is $\pi/\sqrt{12} = 0.91$. Since the coils are handmade, the effective covered area becomes smaller: $A_{eff} \approx 0.8 \cdot 0.12^2 \cdot d \cdot R \approx 0.012 \cdot d \cdot R$.
The effective area is proportional to the number of windings and to the square of the wire radius: $A_{eff} = n\pi r^2$, which leads to $\pi r^2 = 0.012 \cdot d \cdot R/n$.
As the power consumed by the coils is converted to heat it should be minimized:

$$P = R_{el} I^2 = 2n \frac{2\pi R}{\pi r^2} \cdot \rho_{el} I^2 \stackrel{!}{=} \min \tag{3.9}$$

With the equation above and eq.(3.8):

$$P = \frac{4\pi\rho_{el}}{0.012} \cdot \frac{4}{9\mu_0^2} \cdot A^2 \cdot \frac{(R^2 + (d/2)^2)^5}{d^3 R^4} \tag{3.10}$$

As R can always be expressed in terms of d, $P \propto d^3$ is obtained and d is geometrically restricted as above. Setting $\frac{\mathrm{d}}{\mathrm{d}R} P = 0$ gives the condition for minimal power consumption at minimal d: $R = \sqrt{1/6}d$. This is different from $R = \sqrt{1/3}d$, but practically low power consumption is more important than perfect linearity of B. Measurement of the electric resistivity gives $\rho_{el} = 2.3 \cdot 10^{-8}\Omega$m (one third more than pure copper), so the power consumption for a certain magnetic field gradient is:

$$P = \frac{4\pi\rho_{el}}{0.012} \cdot \frac{4}{9\mu_0} \cdot A^2 \cdot 0.13^3 \cdot \frac{(1/6 + 1/4)^5}{1/36} \approx 6.7\mathrm{kW} \cdot A^2 \cdot \mathrm{m}^2\mathrm{T}^{-2} \tag{3.11}$$

Typical magnetic field gradients are ≈ 10-20 Gauß/cm = 0.1-0.2 T/m ⇒ $P = 70-270$W. From (3.8) the necessary nI for these field gradients can be computed:

$$nI \approx 6000 \frac{\mathrm{Am}^3}{\mathrm{Vs}} A \Rightarrow nI = 600 - 1200\mathrm{A} \tag{3.12}$$

The wire used for the windings has diameter $2r = 1$mm, so the effective area consists of about 100 wires (to be precise: 103). Therefore, $I \approx 6 - 12$A and $R \approx 1.9\Omega \Rightarrow \Delta U = 12 - 24$V. The power supply for the coil is generously dimensioned: $I_{max} = 20$A and $U_{max} = 36$V allow magnetic field gradients up to 30Gauß/cm.
Measurement of the temperature on the surface of the coils, when they are isolated from any heat sink except the air circulating around them gave the results in table (3.2).

Table 3.2: Measured properties of a single coil in dependence of current I.

I[A]	2	4	6	8
ΔU[V]	1.9	4.1	6.7	10.8
T_{eq}[C°]	30	50	72	120

This clearly motivates the necessity of an adequate cooling system for the coils, temperatures of more than 120°C at the surface during continuous operation indicate that inside the coils the temperature is much higher. The insulating coating of the wire is specified for 180°C, this is probably reached between the wires!

3.4.2 Cooling system

In the following calculation only one coil is considered, as the coils are identical the results hold for both of them. The cooling of the coil is indirect: the coil is wound on an aluminium disc, which is connected to a water-cooled copper disc. The water-cooling of the disc is realized with a copper tube in which water flows and which is soldered to the disc. Three cooling mechanisms are important: heat conduction from all surfaces to the surrounding air, but this is negligible, heat conduction from the coil wires to the cooling tube and heat transfer by convection from the inner wall of the tube to the cooling water. The formula for convective heat transfer through a surface A_{surf} is ([18]):

$$\dot{Q} = \alpha A_{surf} \cdot \Delta T \tag{3.13}$$

ΔT is the equilibrium temperature difference between surface and coolant and α is the heat transfer coefficient, which is velocity dependent:

$$\alpha(\mathrm{H_2O}) = \left(350 + 2100 \cdot \sqrt{\frac{v}{\mathrm{m/s}}}\right) \frac{\mathrm{W}}{\mathrm{m^2K}} \tag{3.14}$$

The velocity of the coolant can be estimated from Hagen-Poiseuille's law, which gives $\dot{V}$. Dividing $\dot{V}$ by the cross section of the tube πr^2 yields:

$$v = \frac{r^2}{8\eta \cdot l}\Delta p \quad , \text{ with } \Delta p_{max} = 5\text{bar},\ l = 13\text{m},\ \eta = 10^{-8}\text{bar}\cdot\text{s}:\ v = 43\frac{\text{m}}{\text{s}} \tag{3.15}$$

Diameter and length of the tube are 6mm and 500mm respectively, therefore $A_{surf} = 0.01\text{m}^2$.

$$\overset{(3.13),(3.14)}{\Rightarrow} \frac{\Delta T_{wall}}{\dot{Q}} = 0.0075\frac{\text{K}}{\text{W}} \tag{3.16}$$

The conclusion from this is that the wall of the tube has approximately the same temperature as the water in the tube.
Multiplication of (3.15) with the specific heat capacity for water $c = 4.162\ \text{kJ}/(\text{kg}\cdot\text{K})$ and with the cross section of the tube gives a similar measure of the temperature change of the coolant:

$$\frac{\Delta T_{water}}{\dot{Q}} = 0.0002\frac{\text{K}}{\text{W}} \tag{3.17}$$

Calculating the heat conduction from the coils to the tube wall is more complicated, because the heat is not deposited at a single surface of the aluminium disc but at several surfaces. With the heat conduction equation

$$\dot{Q} = \lambda\frac{A_{cross}}{l}\cdot\Delta T \tag{3.18}$$

where λ is the heat conductivity of aluminium ($\lambda_{\text{Al}} = 237\frac{\text{W}}{\text{m}\cdot\text{K}}$), A_{cross} is the cross-section through which the heat is conducted and l is the length of heat conductor, and integration of $\text{d}A_{cross}/\text{d}t$ one obtains:

$$\frac{\Delta T_{coil}}{\dot{Q}} = 0.13\frac{\text{K}}{\text{W}}. \tag{3.19}$$

For the interesting range of $\dot{Q}_{1coil} = 35/135\text{W}$ one finds the coils to be theoretically 5K/18K warmer than the coolant. In the experiment, the difference is about twice as high, which is most probably due to the fact, that the contacts between coil and aluminium or between aluminium disc and copper disc are less than perfect, but compared to the measurement without cooling the coil temperatures are still significantly lower.
Examining (2.35) and (3.9) shows a principal problem: the MOT size is proportional to $1/\sqrt{I}$ but the coil temperature (3.19) grows with I^2. Halving the MOT size demands quadrupling the coil current and hence results in a sixteen fold higher temperature difference!

3.5 ^{40}Ar MOT

3.5.1 Measuring the MOT size

When the optical and magnetic setup were completed, the MOT immediately worked, even though the working parameters (beam size, saturation s_0 and magnetic field gradient) were chosen only according to a rough estimation. A typical image can be seen in fig.(3.5), where the colormap is changed from black-white (CCD) to false color. Here $\delta = 2\pi \cdot 5.7\text{MHz}$ and

$$P_{beam} = 1.12\text{mW} \overset{eq.(2.15)}{\Rightarrow} s_0 = 1.2$$

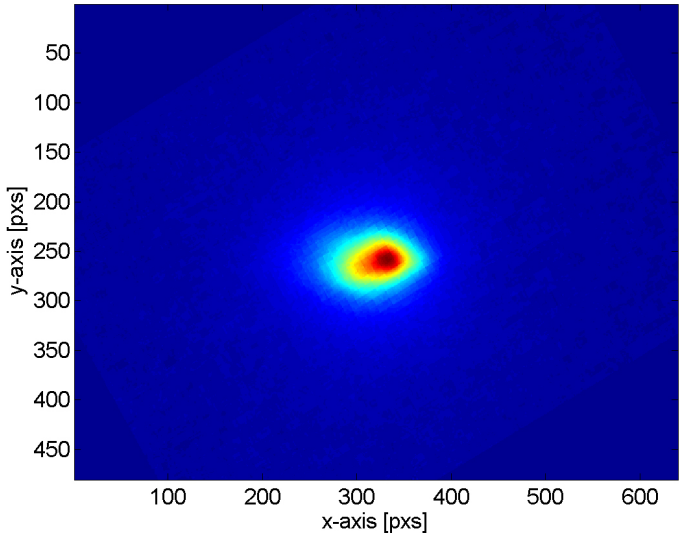

Figure 3.5: The MOT as seen by the CCD, rotated for better analysis.

As the MOT region should be minimal, I is set to 10.0A corresponding (eqs.(3.9),(3.11)) to 17 Gauß/cm gradient and is not changed for any of the measurements below. This is the same for the beam diameter, it is fixed to $\approx$ 10mm.
The size of the MOT is measured with the stripped version of a commercial USB webcam: lens and IR filter are removed and the MOT is directly imaged to the CCD chip. The chip has 480x640 pixels and $\approx$ 2.5x3.2mm^2 area, thus defining the resolution as 5.1μm/px. The MOT is imaged with a f = 80mm lens in d_1=118mm distance and in d_2=285mm distance from the chip surface. Paraxial optic for an object with size g imaged by a lens f to an image size b gives the following expression for d_1 and d_2

$$d_1 = f(1 + \frac{g}{b}),\ d_2 = f(1 + \frac{b}{g}) \tag{3.20}$$

from which the magnification M≡ b/g is calculated as M=2.3. Thus 1 pixel on the CCD corresponds to 2.2μm of the MOT.
There are two parameters whose influence on the MOT size is of interest, namely detuning of the MOT beams and saturation parameter (intensity) of these. It is measured for different detunings (≈3, 6, 9, 12, 17, 22 MHz) and a series with varying s_0 is recorded in each case. The measurement is quite simple: the webcam software allows to record videos, so for each (δ,s_0) set 50 frames are saved. Directly after, a set of 50 dark images is recorded, this allows correction for the background from e.g. the light in the lab. The atom flux is readjusted for each data point to avoid saturation and blooming of the CCD.
A Matlab program was developed which fits a Lorentz profile and a Gaussian to two orthogonal sections through the center of the MOT for each of the frames. The widths of the two fits along the coil axis are used to calculate the MOT size with its standard deviation.

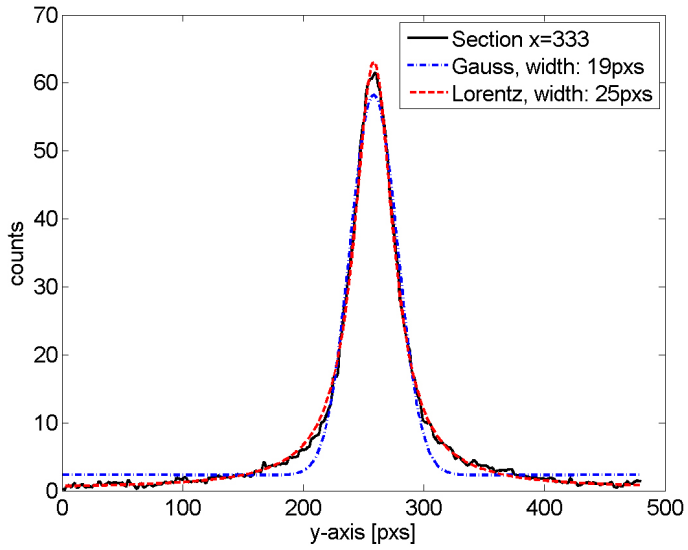

Figure 3.6: Lorentz and Gaussian fit of the section x=333 in fig.(3.5).

Fig.(3.6) clearly shows that the Lorentz curve fits much better to the cut through the twodimensional projection of the MOT, so in the following "MOT size" or z_{rms} refers to the Lorentz width. The subscript rms denotes the root-mean-square, which is for a Gaussian distribution identical to 1σ.

3.5.2 Comparison with theoretical prediction

The results of the measurements described above are illustrated in fig.(3.7), the left-hand graphs show the MOT size for different detunings and s_0's, the predictions according to (2.35) are indicated by the lines. In these predictions, the saturation paramter is set to six times the saturation parameter of one beam, this allows for the extension of the onedimensional model to three dimensions.
From the measured MOT size the measured β is calculated by (2.34),(2.28) and (2.32), it leads with (2.28) to the measured temperature:

$$\beta^{meas} = \sqrt{\frac{D_0^{theo}\hbar k}{\mu' A}} \cdot \frac{1}{z_{rms}^{meas}} \Rightarrow T^{meas} = \frac{1}{k_B} \cdot \sqrt{\frac{D_0^{theo}\mu' A}{\hbar k}} \cdot z_{rms}^{meas} \tag{3.21}$$

These measured temperatures of the MOT can be seen in the right-hand plots. The lines show the predicted temperature $T = D_0^{theo}/(k_B\beta^{theo})$.
The measurements are not in very good agreement with the predictions, except that with $\delta \approx \gamma \approx 6$MHz. In most plots, the data points and the theory have at least the same characteristics, namely sign of the slope and position of the extrem values. One can see, that e.g. z_{rms} is for low detunings a bit bigger than predicted and for high detunings it is much smaller. A possible error lies in the method of measurement itself: the CCD camera automatically corrects its sensitivity in a way, that the brightness of the image is in a certain regime. This can cause problems during data evaluation, because then the dark image is recorded under different operating conditions than the MOT image. Another source of errors is that the linearity of the CCD is unknown, this might decrease the sensitivity in domains where the intensity is high, thus changing the widths of the distributions. By adjusting the flux of atoms so that the peak intensity in the middle of the MOT is always approximately the same and less than saturation one tries to eliminate that effect.
A very grave error is due to exclusive consideration of the Doppler-cooling mechanism and the approximations in the derivation of its characteristics. The deviation to much smaller MOT sizes can be attributed to sub-Doppler cooling mechanisms: the effect of these mechanisms grows with detuning.
All the calculations are based on the assumption, that the beams are perfectly circular polarized, since the waveplates are not optimized for the wavelength in the experiment, so it is well possible that the polarisation is elliptic. This can be expressed in the base of circular polarisations, which leads to an polarisation component orthogonal to the desired one. This is equivalent to heating of the MOT and hence is -besides the one mentioned before- probably the most severe error of all.

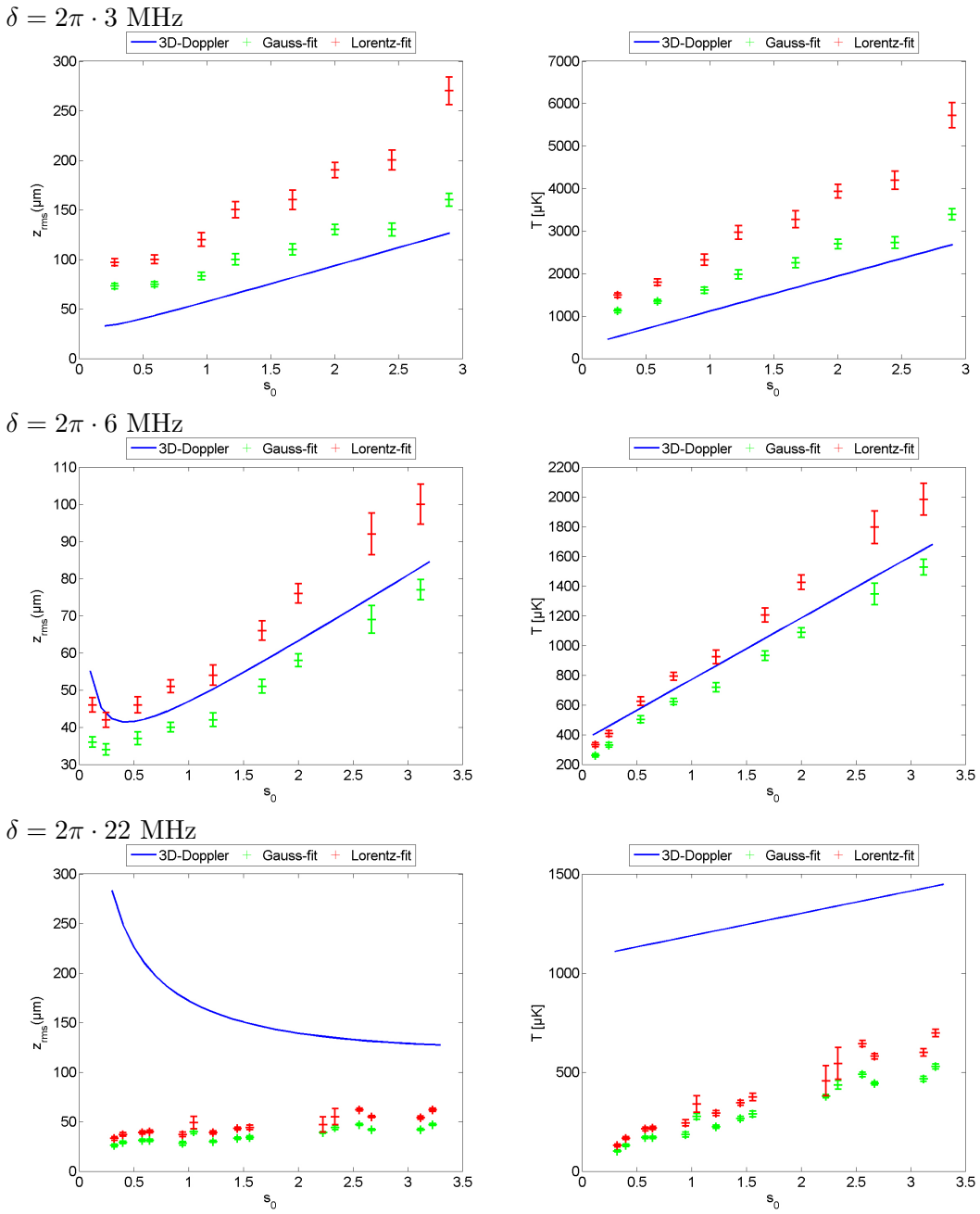

Figure 3.7: MOT size and temperature for different detunings, the solid lines show the theoretical predictions, the green dots show the measurement/ calculation for a Gauss-fit and the red dots show the same for the Lorentz-fit.

4 Single particle detection

4.1 Detection system

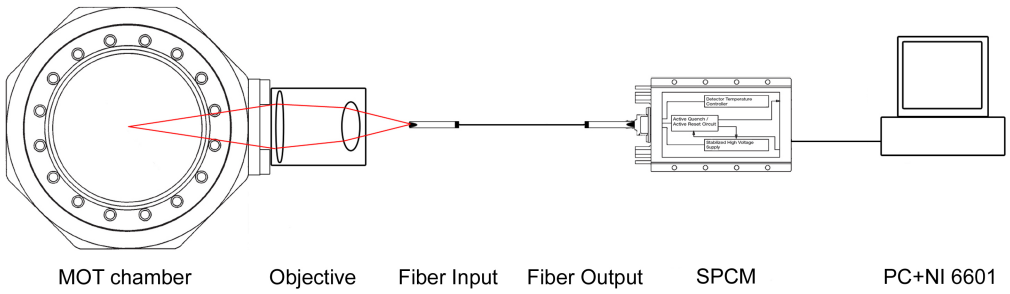

Figure 4.1: The optical setup for fluorescence detection.

4.1.1 Geometrical efficiency

The MOT fluorescence is observed by one of the eight CF40 viewports of the MOT chamber. The percentage of fluorescence that can be collected is limited by the aperture of this orifice: The seal has a diameter of 36 millimeters and is located about 89 millimeters from the chamber center. During assembly of the MOT chamber and test of the detection system several "light-traps" were installed. These are graphite coated metal tubes with 34 millimeters inner diameter and are located in every port of the Kimball except of the two CF100 windows and the two CF40's on the Zeeman slower axis. Length and inner diameter of the tubes are 44 millimeters (from the seal) and 34 millimeters respectively, thus limiting the observable solid angle to $\pi \cdot (34/2)^2/(4\pi \cdot 89^2) = 0.009$. This is later referred to as "geometrical efficiency" η_{geo}.

4.1.2 Fiber coupling

For reduction of background photons and the idea of a plug'n'play setup, the MOT fluorescence is coupled into a multimode FC-APC (angled physical contact) fiber and is transferred to a photon counter. The coupling is done with a commercial TV macroobjective (f=70mm, f/#=1.4) which is not specially coated for 812nm and whose entrance is in 120 mm distance from the MOT center. The objective has four lenses, the typical loss for uncoated glass is 5% per surface, this leads to an overall transmission of 66%. When the objective was tested with a pointlike light source in about 120 mm distance, the entrance aperture was determined to only 24 ± 2 millimeters diameter and the exit numerical aperture to 0.18. The small entrance aperture reduces the geometrical efficiency, but for convenience it is combined with the objective transmissivity to the "objective efficiency" η_{obj}:

$$\eta_{obj} = \frac{((24 \pm 2)/2)^2}{\left(\frac{34/2}{89} \cdot (120 \pm 1)\right)} \cdot 0.95^8 = 0.18 \pm 0.03$$

One of the crucial points in the fluorescence detection is the fact that the image of the MOT is always bigger than the size of the fiber to which it is focused. The fiber core diameter is 62.5μm and the magnification of the objective is estimated to $M = 0.7 \pm 0.1$. A minimal measured MOT diameter ($2R_{MOT} = 4z_{rms}$) of 120μm hence directly leads to an image bigger than the fiber core. This "imaging efficiency" is experimentally obtained by scanning the MOT image with the fiber end: $\eta_{image} = 0.3 \pm 0.1$.
The typical loss in an optical multimode fiber is 50%, this is expressed by the "fiber coupling efficiency" $\eta_{fiber} = 0.5$.

4.1.3 Single photon counter

The multimode fiber is plugged to a Perkin & Elmer single photon counting module SPCM-AQR-13-FC which consists of an avalanche photo diode (APD) that is thermoelectrically stabilised and an electric circuit that levels the APD photon count signals to 5 volt TTL pulses. The counter has a dark count rate of around 300 counts/second, but it is specified to have only around 110 c/s. This difference probably occurs because the SPCM in the experiment is mounted to a simple aluminium plate. It is possible to operate it in a 5°C environment, that should decrease the dark countrate significantly.
Intrinsic dark counts by the detector are of minor importance compared to those occuring from stray light caused by clipping of the MOT beams at the second $\lambda/4$-plates. This clipping is unavoidable due to imperfections in the collimation lenses and due to scratches in the windows. It is already reduced by the light traps by one order of magnitude, but should be brought to a negligible number by coating all inner surfaces of the MOT chamber with non-reflecting graphite. A overall power of about 6mW in the MOT beams (2 passes of 3 beams with 1mW) leads to ≈3000 dark counts per second.
Located in the fiber inlet of the detector there is a GRIN (GRaded INdex) lens which

ensures that light from a 100μm fiber covers the whole 175 μm active area of the APD. The efficiency of the detector at 812nm is found in the datasheet, $\eta_{det} = 0.53$.
Counting of the TTL pulses produced by the SPCM is done with a National Instruments NI-6601 PCI card and the countrate/time unit is recorded to .txt-files with a program written in Labview. Further data processing is done with Matlab.

4.2 Systematic approach to single particle detection

4.2.1 Scattering rate

One single atom scatters photons at the rate γ_p eq.(2.17). The linewidth of the $1s_5 - 2p_9$ transition of Ar is $\gamma = 2\pi \cdot 5.87$ MHz, thus the maximum scattering rate is 18.4 MHz. In eq.(2.17) s_0 has to be replaced by $6s_0$ and this yields with typical δ's $\gamma_p \approx$ 8MHz. Multiplication of this with the total detection efficiency gives the expected photon countrate at the detector and its systematic deviation:

$$\eta_{tot} = \eta_{geo} \cdot \eta_{obj} \cdot \eta_{image} \cdot \eta_{fiber} \cdot \eta_{det} = (1.3 \pm 0.5) \cdot 10^{-4}$$

$$c_{det} = \eta_{tot} \cdot \gamma_p = (1040 \pm 400)\mathrm{s}^{-1} \tag{4.1}$$

Measuring with 40ms time resolution leads to a signal height of 42 ± 16 counts while $\sim 100 \pm 10$ dark counts are expected in the same time period.

4.2.2 Detectibility

Information about the variation of the MOT size with s_0 and δ can be used to locate a first set of parameters where single atom fluorescence can be observed. This is done by defining the detectibility Δ. As the photon scattering rate and the area covered by the MOT image at the entrance of the fiber are the most relevant variables in the experiment, a simple approach to Δ is: $\Delta = \gamma_p / z_{rms}^2$. z_{rms} is directly proportional to its image, the proportionality factor is the optical magnification M. γ_p can be calculated from theory, but as the measurement of z_{rms} shows significantly different behaviour than the prediction, the measured z_{rms} are those one relies on when calculating Δ.
As the MOT size was determined for $\delta = 3, 6, 9, 12, 17$ and 22 MHz one can compare the detectibilities for all these detunings in individual dependence on s_0. These results are illustrated in fig.(4.2).
For all detunings the detectibility is maximal near $s_0 = 1$. The value of this maximum for one detuning peaks at a detuning of $\delta = 9$MHz, $\Delta(9\mathrm{MHz}, s_0 = 0.8) \approx 9 \cdot 10^{15}\mathrm{Hz/m}^2$. This value is about four times bigger than the one at 22MHz and s_0=1.2, where initial measurements took place and did not yield satisfying results.
From the section above, one expects the countrate to be there maximally 10 counts per atom in 40 ms. As the saturation parameter at which the maximum detectibility lies increases with detuning, the necessary s_0 at 22MHz should be bigger than at 9MHz.

$\delta = 2\pi \cdot 3$ MHz

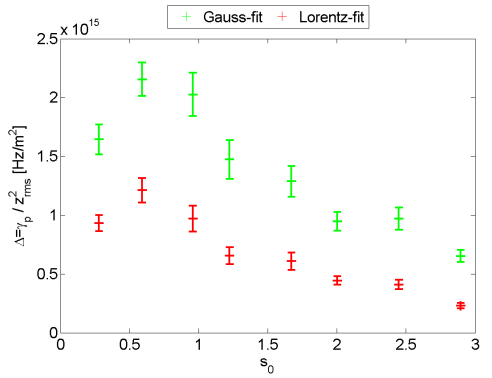

$\delta = 2\pi \cdot 6$ MHz

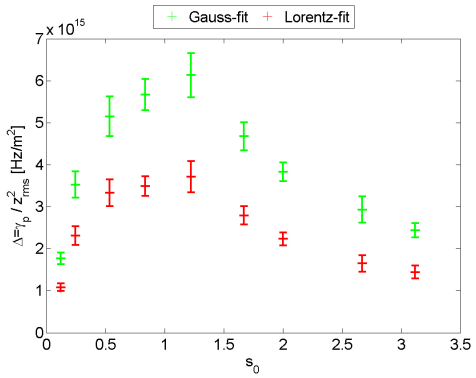

$\delta = 2\pi \cdot 9$ MHz

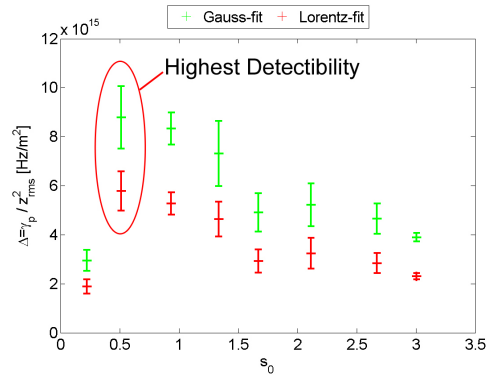

$\delta = 2\pi \cdot 12$ MHz

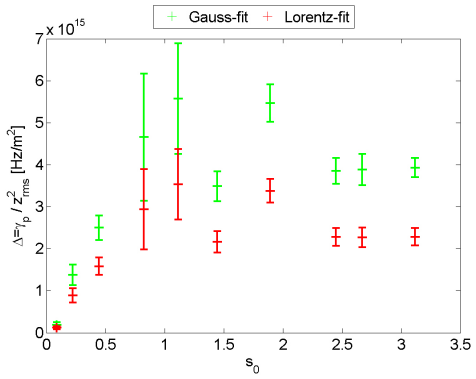

$\delta = 2\pi \cdot 17$ MHz

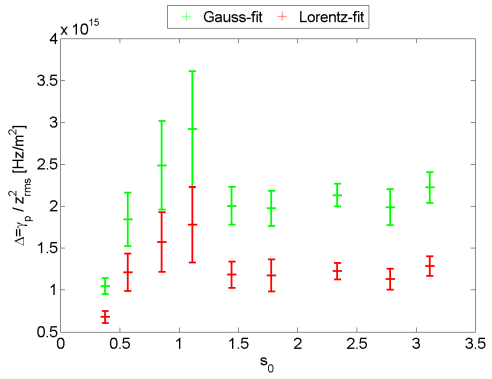

$\delta = 2\pi \cdot 22$ MHz

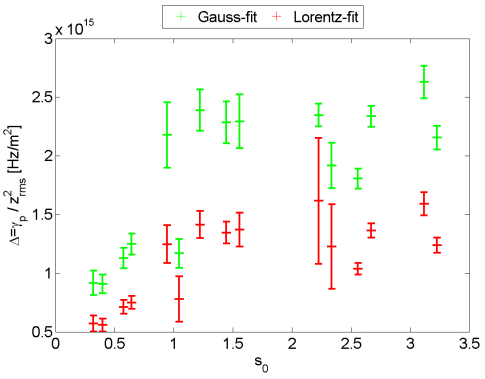

Figure 4.2: Detectibility for different detunings, the green dots show the measurement/ calculation for a Gauss-fit and the red dots show the same for the Lorentz-fit. The highest detectibility is expected at $\delta = 9$ MHz and $s_0 = 0.5$.

This leads to a higher dark countrate and hence explains why nothing was observed at 22 MHz: 10counts/40ms signal are extinguished by at least 10counts/40ms noise on the dark counts.

4.3 First signal

After adjusting the apparatus to the right parameters, the detection of single atom fluorescence was successful. The recorded signals are fluorescence counts as a function of time, for evaluation purposes it is also plotted as normalized histogram: probability of signal height as function of signal height.

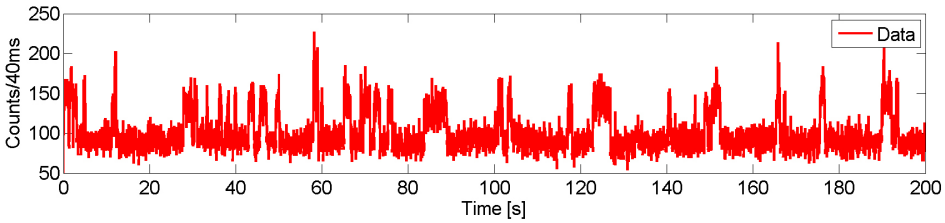

Figure 4.3: Plot of the signal vs. time as recorded by the SPCM.

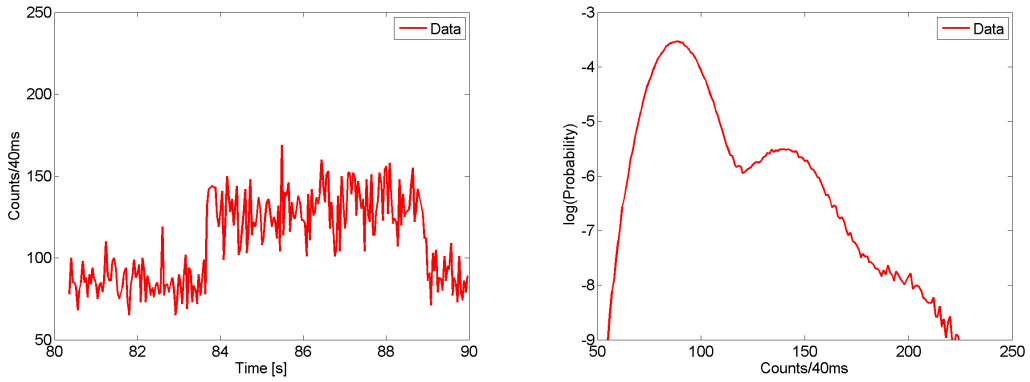

Figure 4.4: Zoom of fig.(4.3) and histogram plot with logarithmic scale.

One can clearly see, that the fluorescence signal height alternates between different quite discrete values. There is an background/ dark countrate and on top of it are boxlike structures. The boxes have all the same average height (average over the length of the boxes) or integer multiples of this height.
A histogram of the data clarifies this: the first peak is the background with its gaussian distribution (parabolic in log. scale), the second peak is the background plus one box height. The peak for background plus two box-height's is also visible though not as

pronounced.
The second peak is now identified with one atom in the MOT. This is reasonable, because first of all it is a discrete peak, secondly it is about 55counts/40ms away from the dark count peak and thus in good agreement with the prediction and thirdly there is a hill-like structure in 40-60 counts distance at the descending flank of it. This third maximum indicates that there are sometimes two atoms at the same time in the MOT. The heights of the peaks depend on the flux of atoms, higher flux makes the "zero atom" situation less probable and increases the probabilities for higher atom numbers in the MOT. The logarithmic histogram for such a higher Ar flux is shown below in fig.(4.5).

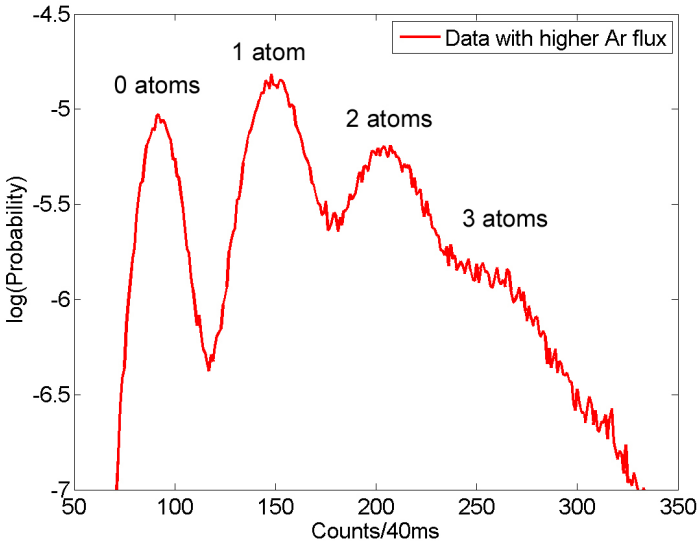

Figure 4.5: Histogram plot for higher Ar flux with logarithmic scale.

4.4 Signal quality

4.4.1 Overlap and trigger

The signal quality can be quantified by the probability to falsely count zero atoms as one atom. This is illustrated in fig.(4.6): two gaussians, which are separated by a not to big gap have a measurable overlap. On the one hand, one does not want to lose atoms by counting "ones" as "zeros". On the other hand, counting "zeros" as "ones" has to be avoided. The first criterion is met by accepting all counts above $\mu_1 - 3\sigma_1$ as "ones". The second is fulfilled by establishing a trigger t: due to the frist criterion, there is a certain probability p to count a "zero" as a "one" which is given by the gray area in the figure. As it is always smaller than unity a certain number t of consequent counts right

of the parting line ensures that the miscount probability p_{mis} is sufficiently small. Calculation of p and t is done in the following way:

$$p = \mathrm{Erf}\left(\frac{\mu_1 - \mu_0 - 3\sigma_1}{\sqrt{2}\sigma_0}\right) \text{ and } p^t \leq p_{mis} \Rightarrow t = \frac{\log(p_{mis})}{p} \tag{4.2}$$

A typical histogram (δ = 6MHz, P=0.83mW) from a series of measurements is also

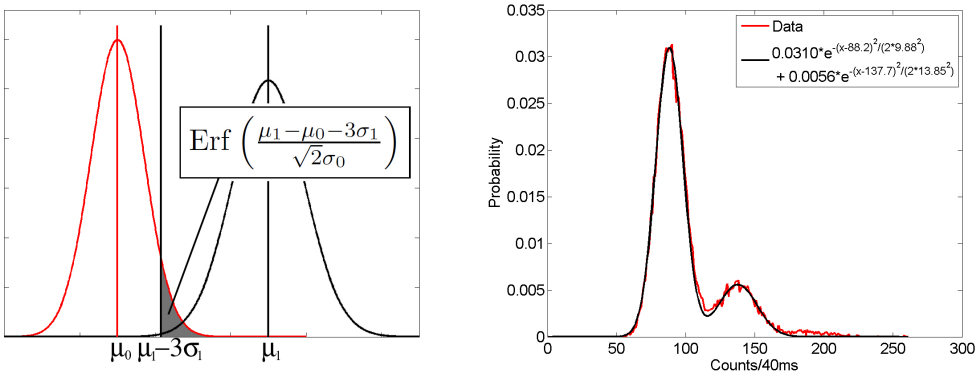

Figure 4.6: Illustration of the overlap probability and a measured example.

plotted in fig.(4.6). The two fitted gaussians are added, that helps to compare fit and data. In that case the overlap probability is 0.25. Setting the certainty for detection to $1 - p_{mis} = 99.9\%$ leads to a trigger of 5 times the integratio time, as the integration time is 40ms one atom has to be detected for 0.2s in the MOT to assure that it is really an atom.
The complete results for all measured detunings and beam powers are in table(4.1). When the overlap between the two gaussian becomes too big, a very long trigger time is necessary, making those parameter sets (δ, $s_0 \hat{=} 1.11 \cdot P[\mathrm{mW}]$) unfavorable. The best signal quality is reached for (6MHz, 0.44mW) and (9MHz, 0.83mW) where the probability to falsely count a "zero" as a "one" is 0.17 and 0.25 respectively.
Comparing the μ's to the σ's one can clearly see, that for low intensities the noise becomes nearly poissonian, while at higher intensities the variation of the laser power that increases linearly becomes dominant.

4.4.2 Single atom lifetime and detection probability

The recorded fluorescence signal also contains information about the lifetime of a single atom in the MOT. Access to that information is granted if the lengths of single atom counts are statistically evaluated. The Matlab program written for this operation first smoothes the fluorescence-over-time signal to cancel out statistical short time fluctuations of the countrate. It then searches the points where the smoothed signal starts to

Table 4.1: Measured values for signal quality analysis. The cells with "-" indicate that the overlap of the distribution is too large, making the trigger time too long.

δ[MHz]	P[mW]	μ_0	σ_0	μ_1	σ_1	p	t[s]	τ[s]	$\Delta\tau$[s]	p_{det}
6.0	0.30	49.0	7.3	87.8	11.1	0.28	0.22	1.06	0.06	0.81
6.0	0.44	59.8	8.1	106.0	12.5	0.17	0.15	1.03	0.06	0.86
6.0	0.64	74.5	9.3	121.0	15.8	0.62	0.57	1.05	0.08	0.58
6.0	0.83	91.4	10.5	133.0	19.1	0.96	-	0.90	0.05	0.00
6.0	1.01	106.0	11.3	133.0	25.1	1.00	-	0.70	0.03	0.00
7.5	0.30	46.4	7.0	76.0	10.8	0.70	0.79	0.81	0.05	0.38
7.5	0.44	61.0	8.1	102.0	12.6	0.42	0.32	1.07	0.08	0.74
7.5	0.64	73.9	9.2	117.0	14.3	0.57	0.50	1.01	0.10	0.61
7.5	0.83	93.1	10.5	140.0	18.1	0.80	1.26	1.02	0.08	0.29
7.5	1.01	108.0	11.4	147.0	23.5	1.00	-	0.77	0.02	0.00
9.0	0.44	59.9	8.0	93.3	11.1	0.55	0.46	0.97	0.07	0.62
9.0	0.64	74.5	9.3	112.0	16.2	0.91	2.91	0.88	0.06	0.04
9.0	0.83	88.2	9.9	138.0	13.9	0.25	0.20	1.05	0.08	0.83
9.0	1.01	112.0	11.6	164.0	18.6	0.70	0.78	0.93	0.04	0.44
9.0	1.35	140.0	14.2	183.0	23.9	0.99	-	0.61	0.02	0.00
12.0	0.83	87.9	9.9	121.0	15.7	0.94	4.37	1.26	0.12	0.03
12.0	1.01	111.0	11.7	149.0	18.7	0.96	-	0.79	0.06	0.00
12.0	1.35	141.0	13.3	184.0	21.0	0.95	-	0.71	0.03	0.00
12.0	1.83	177.0	15.3	222.0	28.0	1.00	-	0.71	0.04	0.00

be bigger than a certain threshold and measures the time until the signal is below that level again. The positions of the "boxes" are saved with lengths. From that a histogram is plotted and an exponentially decaying curve is fitted to it. The lifetime of that decay curve is identical with the expectation value for the lifetime of the atoms and can be found next to its 1σ-error in the τ-column of tab.(4.1).
Typically the histograms are quite jagged because the time to get enough single atom signals at a flux low enough to keep the two-atom situation unprobable is naturally much longer than the time necessary for a signal histogram. For good signal length measurement the estimated time is at least one hour.
In fig.(4.7) the histogram of the signal length at 9MHz and 0.83mW is shown. The integral over the fitted exponential curve is unity and thus allows calculation of the detection

probability p_{det}. This is the fraction of atoms with a lifetime longer than the calculated trigger and hence gives the fraction of atoms that can be unmistakenly identified as atoms. The maximum detectable fraction of atom in tab.(4.1) is 86%.

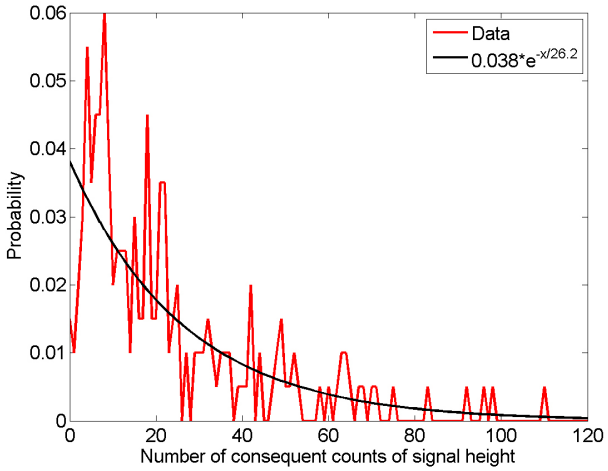

Figure 4.7: Signal length histogram for (9MHz, 0.83mW).

4.5 Optimum parameters of operation

4.5.1 Single atom detection

The optimum detuning and saturation parameter for detection of single atom fluorescence are explained in the section above. Besides those two variables one can also vary beam size and magnetic field gradient. In eq.(2.35) one finds the MOT size to be proportional to $1/\sqrt{A}$ which motivates a high gradient during detection. The beam size has to be small because small beams with a certain intensity create much less stray light than large beams with the same intensity. For detection of atoms in the MOT the beams can have even 1mm diameter because the MOT diameter is maximally of that size.

4.5.2 Single atom capture

Capturing of a high number of atoms from an atomic beam with a certain size works best when the MOT beams have large diameter and high power. In that case, the MOT has a large capture area and the atoms are rapidly driven to its center. As the capture area also depends on the magnetic field gradient via the Zeeman shift one chooses a relatively small gradient. A high number of atoms captured from the atom beam is equivalent to a high probability to capture one distinguished single atom from the beam.

When these capture efficiency considerations come into play there is one more parameter that characterizes the MOT: the loading rate k_{load}. It is defined as the rate -in units of atoms- by which the MOT grows when switched on. This measurement can be experimentally combined with another one: periodic blocking and releasing of the atom beam (in this case the Zeeman slower) gives information about loading rate and lifetime of the MOT. Once the atom beam is blocked, the MOT loses atoms e.g. by two body losses and therefore the number of atoms decays. The decay is not exponential over the whole decay time but as exponential fits can be made for all parameter sets, one obtains comparable information. A typical signal from which the loading rate and the decay time can be derived is plotted in fig.(4.8). The upper figure shows the periodicity of the blocking, the lower one is a zoom where one can see the linearity of the loading and the exponential nature of the decay.
In the experiment, the Zeeman slower is manually blocked and unblocked for about ten to fifteen times per parameter set ($\delta, s_0 = 1.1 \cdot P[\mathrm{mW}]$). The MOT beams are not blocked, this allows continuous measurement of the MOT fluorescence. To make the loading rates comparable, the flux of atoms has to be constant for all points and hence the Zeeman slower detuning has to be readjusted when the detuning is changed. As the countrate per captured atom is known over the range of parameters, the fluorescence (per time unit) can be divided by that number. One obtains the loading rate in atoms/time unit from the ascending slope of the graph.

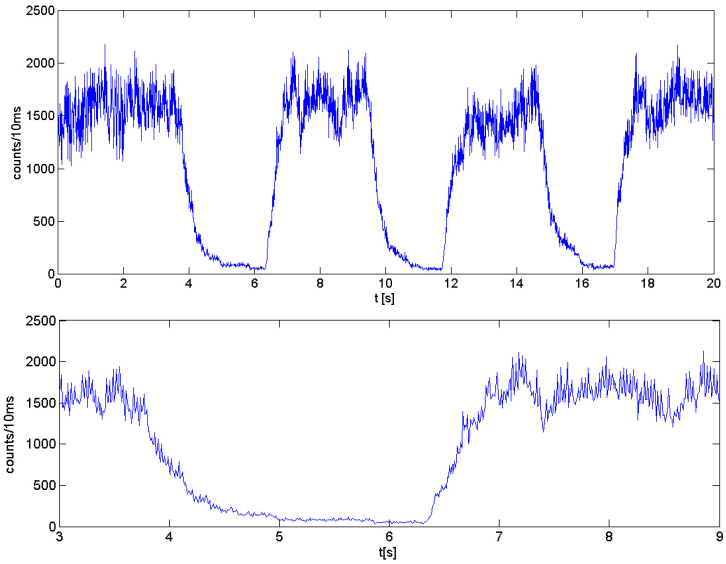

Figure 4.8: The fluorescence signal during the loading rate measurement.

The measured loading rates are illustrated in fig.(4.9). Three points are marked in the figure, they indicate the two parameter sets with highest signal quality (6MHz,

0.44mW) and (9MHz, 0.83mW) and the point where the highest loading rate was measured (12MHz, 2.83mW). For each of these points an image of the MOT is given, this clarifies that although the signal quality at (6MHz, 0.44mW) and (9MHz, 0.83mW) is similar, the MOT size does not have to be same. The similar signal quality is thus an effect of both the scattering rate and the MOT size.

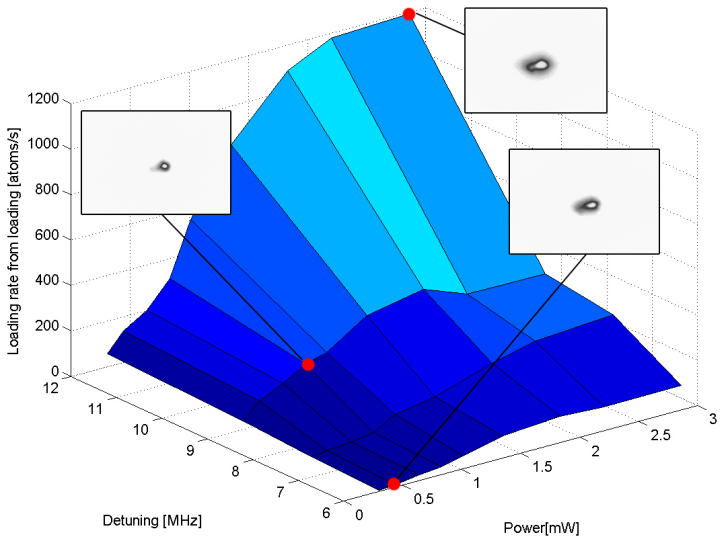

Figure 4.9: Loading rate as a function of δ and P. The points with highest detection probability and the point of highest loading rate are indicated with their MOT image.

For every detuning the loading rate goes to saturation at a certain power and this saturation loading rate increases strongly with detuning. It has to saturate for large detunings, because maximally the complete flux of atoms passing the MOT beams can be captured, but this is subject to future measurements.
The parameters for loading of the MOT and detection of atoms are summarized in table(4.2). As the parameters are substantially different, it has to be switched between them. The future cycle will be the following: In a loading sequence, atoms are captured from a large region in a large MOT. Then the MOT is squeezed by increasing the magnetic field and changing δ and s_0. The beam diameter is also reduced to decrease the background count rate. Afterwards the counter is opened and fluorescence is recorded.

Table 4.2: Parameters for the two modes of operation.

Operation	s_0	Beam	grad(B)	δ	Counter	Δ	k_{load}
Loading	high	large	small	high	blocked	low	high
Detection	low	small	large	low	opened	high	low

5 Summary and outlook

5.1 Resume

The main goal of this thesis is the indirect detection of single metastable ^{40}Ar atoms. The first step towards it is the choice of an additional vaccum chamber that is attached to the existing argon beam machine. As the existing apparatus features an atomic funnel, which is nothing else than a two dimensional magnetooptical trap, the funnel beam is split into four with a compact fiber optical device. These beams are used for the MOT that is built in the center of the new chamber. A pair of coils generates the magnetic field necessary for trapping. Since single atom detection is the aim, the efficiency of the machine is reduced.
In-depth analysis of the MOT with a CCD camera results in the successful choice of parameters that allow capturing and detection of single atoms. In a second series of measurements the performance of the setup is examined with an APD that is sensitive to single photons. Properties like signal-to-noise, loading rate and single atom lifetime are analysed.
The measurements give information about the best mode of operation of the machine. It turns out that it has to be switched between different sets of parameters, because for low loss a high capture efficiency is needed which unfortunately causes low signal quality. By this, the limits of the present setup are found and quantified. As future experiments require higher efficiency and higher signal quality, some features of a new setup are sketched below.

5.2 Capturing ^{39}Ar

In the following an introduction to problems that have to be solved in the future to allow an efficient capturing and counting of ^{39}Ar is given. Some of the depicted techniques are already explicitly planned and some are even currently set up while others are still in an early design stage.

5.2.1 Availability

As already mentioned before argon has several rare isotopes of which ^{39}Ar is of special interest, because it may give access to information about the age of a water sample [3]. The problem is the low natural concentration: in a natural surface water sample every $4 \cdot 10^{21}$th particle is ^{39}Ar.
The total capture efficiency of the machine is 10^{-7}, as 10^{18} atoms are put in per second and the proportion of ^{39}Ar in total argon is $\approx 10^{-15}$ one expects 1 atom in the MOT in three hours. Therefore it is clear that natural samples can hardly be used to adjust the apparatus to highest efficiency which yields need for enriched samples.
Gas samples rich in ^{39}Ar can be made in neutron reactors by ^{39}K(n$_{fast}$,p)^{39}Ar [21]. In the present case rock with 10% K content is enriched in the neutron reactor in Geesthacht. Due to the limited sample volume and the relatively low flux of fast neutrons the total number of available ^{39}Ar atoms is estimated to $\approx 1.4 \cdot 10^{15}$ corresponding to $5 \cdot 10^{-5}$ccSTP, where ccSTP denotes cubic centimeters at standard pressure and temperature (1bar, 273.15K).
The rock is outgassed in an oven afterwards. It releases its gas content and the gas is processed to obtain a nearly pure ^{39}Ar sample (maximally 5% Ar-40 and Ar-38). By freezing the atoms to cold active coal in an evacuated transport container it is transferred to a spectroscopy cell. The cell has approximately 15 cm^3 volume, thus the ^{39}Ar partial pressure is $\sim 4 \cdot 10^{-3}$mbar.

5.2.2 Hyperfine structure

^{39}Ar does not only have a different nuclear mass than ^{40}Ar that leads to isotope shifts of the transition frequencies. It also has a non-zero nuclear magnetic moment so the Zeeman levels show hyperfine splitting. This is the second reason besides the low availability why the spectroscopy of ^{39}Ar is much complicated than the spectroscopy of ^{40}Ar.
The cooling and trapping transition is the same as for ^{40}Ar: $1s_5$(J=2)-$2p_9$(J=3). This is different from that in [22] where $1s_5$(J=2)-$2p_3$(J=2) is examined (fig.(3.1)). But the transitions are similar and since no hyperfine data on the present transition is available, one may use the isotope shift for $1s_5$-$2p_3$ as an estimate.
The hyperfine splitting of the levels is calculated with the hyperfine formula and the magnetic dipole and electric quadrupole moments, that are expressed in the hyperfine factors A and B:

$$\Delta E = \frac{1}{2}AC + \frac{B}{4}\frac{\frac{3}{2}C(C+1) - 2I(I+1)J(J+1)}{I(2I-1)J(2J-1)} \tag{5.1}$$

where J is the total angular momentum quantum number, $I = +\frac{7}{2}$ is the nuclear spin of ^{39}Ar, F is the coupling of J and I and C is $F(F+1) - I(I+1) - J(J+1)$.
A and B for $1s_5$ and $2p_3$ can also found in [22] and one transfers once again the values from $2p_3$ to $2p_9$. The resulting shift of the transitions frequencies is illustrated in fig.(5.1). The

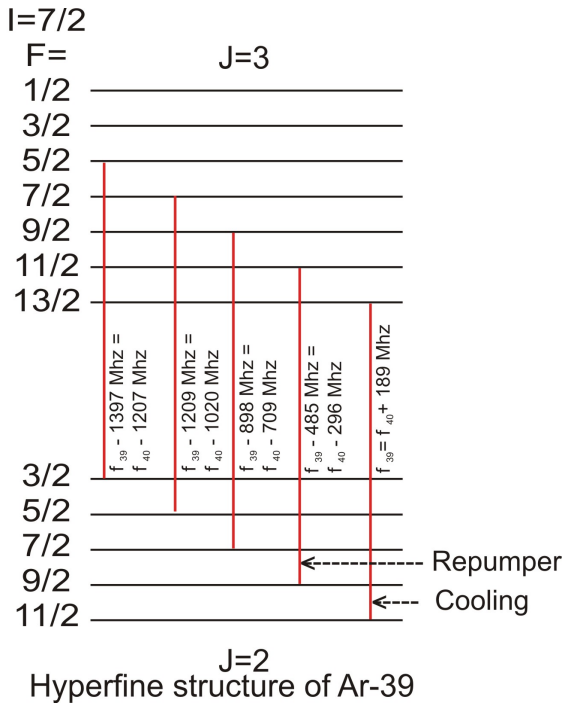

Figure 5.1: Hyperfine levels and transition frequencies for Ar-39.

shifts are given relative to $1s_5 - 2p_9$ of ^{40}Ar and relative to $1s_5(11/2) - 2p_9(13/2)$. Two transitions are denoted with names "Cooler" and "Repumper", because atoms in the upper level of the cooling transition have a small probability to decay to different lower levels, on which the cooler does not work any more and the atom is "lost". Therefore, repumping to one of the upper levels is needed.
The bottom line of the last three paragraphs lies in the information, that the expected deviations of the required frequencies are all only a few hundreds of MHz away from the spectroscopically easy ^{40}Ar line. If the differences are to be exactly known the spectroscopy cell comes into play. Spectroscopy of ^{39}Ar and comparison with ^{40}Ar yields the necessary knowledge and the laser can be simply shifted in frequency away from the ^{40}Ar line by AOMs.

5.2.3 Implications for a new setup

A new experimental setup for ^{39}Ar detection is not completely different from the old one, but there are certain improvements. The two most crucial factors that influence the design are the overall source-detector efficiency (η_{sd}) and directly affected by it the sample consumption.
Low η_{sd} leads to long run time: capturing 10^{-4} ^{39}Ar atoms per second with 10% precision

(shot noise), i.e. 100 atoms captured, yields roughly 12 days sequence time. The input is 10^{18} argon atoms per second. As one liter of groundwater contains approximately 10^{19} argon atoms, 100 000 liters of water have to be processed per sample which is far above practically possible sampling.
Recycling of all the gas that is pumped away between intake and MOT chamber decreases this number drastically. The efficiency between source and MOT is calculated to be less than 10^{-7}, therefore every atom can be recycled about 10 000 000 times before being detected. That brings the sample consumption to nearly zero, one needs only enough argon gas to fill the complete cycle once (this holds only for the ideal case of 100% recycling efficiency). If the cycling time is 100 seconds, which is probably a too high number, 10 liters of water sample are necessary.
Improvements in the excitation efficiency of the source do not affect the input: one can assume that only a small fraction of the strongly dominating ^{40}Ar atoms reaches the MOT. As they do not interact with the laser, it does not matter whether they are metastable or not. That means that the ^{39}Ar* flux can be selectively boosted and thus the sequence time can be reduced by increasing the efficiency of the source. Since this has not been closely looked at in the present setup it bears the chance of great enhancement.
Another aspect that becomes important in a new design is the detection system. The present one has a low efficiency of only $(1.3 \pm 0.5) \cdot 10^{-4}$. Most of the partial efficiencies are fixed, but the objective efficiency $\eta_{obj} = 0.18 \pm 0.03$ still affords the opportunity of improvement. A new lens system is already designed in OSLO and its efficiency is estimated (aperture reduction $\cdot$ transmisson) to $\eta'_{obj} = 0.66$. It is also well possible that it increases the imaging efficiency, because the better lenses create a less smeared out image. η_{image} can also be increased by using a fiber with a bigger core, one can change the 62.5μm fiber to 105μm.
As already motivated above, large profit may be expected from reducing the reflectivity of the inner surfaces of the MOT chamber. At the moment they are polished stainless steel “mirrors”, graphite coating is much less reflective.
These modifications hopefully lead to much better signal quality and thus decrease the trigger time for the desired certainty of detection. This automatically increases the detection probability and helps to reduce the sequence time.

Bibliography

[1] H. Oeschger, A. Gugelmann, H. Loosli, U. Schotterer, U. Siegenthaler, W. Wiest, Argon-39 dating of groundwater, Isotope Techniques in Groundwater Hydrology, Proc. Symp. Vienna, IAEA, Vienna, 1974

[2] H.H. Loosli, A dating method with ^{39}Ar, Earth and Planet. Sci. Lett. 63 51, 1983

[3] H.H. Loosli, Applications of ^{37}Ar, ^{39}Ar and ^{85}Kr ind hydrology, oceanography and atmospheric studies, "Isotopes of noble gases as tracers in environmental studies", pp. 73-85, IAEA, Vienna,

[4] W.G. Mook: Environmental Isotopes in the Hydrological Cycle, Vol. I, http://www.iaea.org/programmes/ripc/ih/volumes/volumes.htm, 2000

[5] H.H. Loosli, M. Moell, H. Oeschger, U. Schotterer, Ten years low level counting in the underground laboratory in Bern, Switzerland, Nucl. Instrum. Methods Phys. Res. B17 402, 1986

[6] Z.T. Lu, K. Bailey, C.-Y. Chen, X. Du, Y.-M. Li, T.P. O'Connor, L. Young, Atom Trap Trace Analysis, Hyperfine Interact., 127, 515-518, 2000

[7] C.-Y. Chen, Y.-M. Li, K. Bailey, T.P. O'Connor, L. Young, Z.T. Lu, Ultrasensitive Isotope Trace Analysis with a Magneto-Optical Trap, Science, Vol. 286, p. 1139-1141, 1999

[8] N.C. Sturchio, X. Du, R. Purtschert, B.E. Lehmann, M. Sultan, L.J. Patterson, Z.-T. Lu, P. Müller, T. Bigler, K. Bailey, T.P. O'Connor, L. Young, R. Lorenzo, R. Becker, Z. El Alfy, B. El Kalioubly, Y. Dawood, and A.M.A. Abdallah, One million year old groundwater in the Sahara revealed by krypton-81 and chlorine-36, Geophys. Res. Lett., 31 (L05503), doi:10.1029/2003GL019234, 2004.

[9] H. J. Metcalf, Peter v.d. Straaten: Laser Cooling and Trapping, Springer-Verlag, New York, 1999

[10] C. Cohen-Tannoudji, B. Diu, F. Laloe, Quantum Mechanics Vol. 1+2, Wiley Interscience, 1977

[11] J. Dalibard, C. Cohen-Tannoudji, Laser cooling below the Doppler limit by polarization gradients: simple theoretical models, J. Opt. Soc. Am. B 6, 2023- (1989)

[12] P. J. Ungar, D. S. Weiss, E. Riis, and S. Chu, Optical molasses and multilevel atoms: theory, J. Opt. Soc. Am. B 6, 2058- (1989)

[13] Particle Data Group, 2002, http://pdg.lbl.gov/2002/clebrpp.pdf

[14] H. Haken, H.C. Wolf: Atom- und Quantenphysik, 2000, Springer-Verlag, Berlin/Heidelberg

[15] Ralchenko, Yu., Jou, F.-C., Kelleher, D.E., Kramida, A.E., Musgrove, A., Reader, J., Wiese, W.L., and Olsen, K.: NIST Atomic Spectra Database (v. 3.1.2), [Online]: http://physics.nist.gov/asd3, 2007

[16] M.Störzer: Realisierung eines langsamen, intensiven Strahls metastabiler Argonatome, diploma thesis, Konstanz, 2003

[17] W. Demtröder: Laser spectroscopy: basic concepts and instrumentation, Springer-Verlag, Berlin/Heidelberg, 1998

[18] Lehrstuhl für Wärme- und Stoffübertragung, RWTH Aachen, lecture "Wärme- und Stoffübertragung", 2006, http://www.wsa.rwth-aachen.de

[19] P. Collon, W. Kutschera, and Z.-T. Lu, Tracing Noble Gas Radionuclides in the Environment, Annu. Rev. Nucl. Part. S., 54, 2004.

[20] P. Collon, M. Bichler, J. Caggiano, L. DeWayne Cecil, Y. El Masri, R. Golser, C.L. Jiang, A. Heinz, D. Henderson, W. Kutschera, B.E. Lehmann, P. Leleux, H.H. Loosli, R.C. Pardo, M. Paul, K.E. Rehm, P. Schlosser, R.H. Scott, W.M. Smethie, and R. Vondrasek, Development of an AMS method to study oceanic circulation characteristics using cosmogenic ^{39}Ar, Nucl. Instr. and Meth. in Phys. Res. B, 223-224, 428-434, 2004

[21] W.A. Traub, F.L. Roesler, M.M. Robertson, and V.W. Cohen, Spectroscopic Measurement of the Nuclear Spin and Magnetic Moment of 39-Argon, Journal of the Optical Society of America 57, pp. l452–1458, 1967

[22] A. Klein, B.A. Brown, U. Georg, M. Keim, P. Lievens, R. Neugart, M. Neuroth, R.E. Silverans, L. Vermeeren and ISOLDE Collaboration, Moments and mean square charge radii of short lived argon isotopes, Nucl. Phys. A, 607, pp.1-22, 1996

A Acknowledgements

This section is dedicated to all those who supported me knowingly or unknowingly during my studies and especially in the last nine months.
I would like to thank

- Markus Oberthaler and Werner Aeschbach-Hertig for supervising and grading my diploma work, productive discussions, knowledge and for giving me the opportunity to continue my work on the project
- Elisabeth Kierig for introducing me to the experiment, many answers, the funny time in the lab and for patiently letting me unlock lasers ;-)
- Arne Schietinger and Jiří Tomkovic for the cooperation in the lab, good discussions, cheering up the time in the office, correcting the thesis and for until now nine very cool months.
- Anna Wonneberger for productive questioning my work and the project, creative input, revising this thesis and up to now a good time
- Jens Appmeier, Jérôme Estève, Rudolf Gati, Stefano Giovanazzi, Christian Groß, Dagmar Hufnagel, Karsten Joho, Jan Krieger, Peter Krüger (special thanks for the detailed feedback), Eike Nicklas, Marc Repp, Stefan Weiß, Andreas Weller and Tilman Zibold for being members of the group, helping me whenever I had questions, the atmosphere in the group and for all the breakfasts, coffee-breaks, barbecue evenings and poker nights
- All members of the workshop, especially Siegfried Spiegel for introduction to the machines and many solutions for mechanical problems
- Elisabeth Holz for being part of my life and letting me be part of hers
- Michael, Renate, Angelika and Kristina Welte for 25 years of support
- My friends for being my friends
- The Erasmus program for letting me study life rather than physics
- SoaD, Knorkator, Thumb, VP-1, Everlast, M. Manson, Korn, Green Day, Rage,...

Declaration:

I hereby confirm that I wrote this thesis on my own and that I did not use other sources or means than stated.

Heidelberg, the _____ _____

Signature